





# Characterizing the assembly of dark matter halos with protohalo size histories: I. Redshift evolution, relation to descendant halos, and halo assembly bias

Kai Wang <sup>1,★</sup> H.J. Mo,<sup>2</sup> Yangyao Chen <sup>3,4</sup> Huiyuan Wang <sup>3,4</sup> Xiaohu Yang,<sup>5,6,7,8</sup>  
Jiaqi Wang,<sup>5,6</sup> Yingjie Peng,<sup>1,9</sup> Zheng Cai <sup>10</sup>

<sup>1</sup>Kavli Institute for Astronomy and Astrophysics, Peking University, Beijing 100871, China

<sup>2</sup>Department of Astronomy, University of Massachusetts Amherst, MA 01003, USA

<sup>3</sup>School of Astronomy and Space Science, University of Science and Technology of China, Hefei, Anhui 230026, China

<sup>4</sup>Key Laboratory for Research in Galaxies and Cosmology, Department of Astronomy, University of Science and Technology of China, Hefei, Anhui 230026, China

<sup>5</sup>Department of Astronomy, School of Physics and Astronomy, Shanghai Jiao Tong University, Shanghai 200240, China

<sup>6</sup>Shanghai Key Laboratory for Particle Physics and Cosmology, Shanghai Jiao Tong University, Shanghai 200240, China

<sup>7</sup>Tsung-Dao Lee Institute, Shanghai Jiao Tong University, Shanghai, 200240, China

<sup>8</sup>Key Laboratory for Particle Physics, Astrophysics and Cosmology, Ministry of Education, Shanghai Jiao Tong University, Shanghai 200240, China

<sup>9</sup>Department of Astronomy, School of Physics, Peking University, 5 Yiheyuan Road, Beijing 100871, People's Republic of China

<sup>10</sup>Department of Astronomy, Tsinghua University, Beijing 100084, China

Last updated 2020 May 22; in original form 2018 September 5

## ABSTRACT

We propose a novel method to quantify the assembly histories of dark matter halos with the redshift evolution of the mass-weighted spatial variance of their progenitor halos, i.e. the protohalo size history. We find that the protohalo size history for each individual halo at  $z \sim 0$  can be described by a double power-law function. The amplitude of the fitting function strongly correlates to the central-to-total stellar mass ratios of descendant halos. The variation of the amplitude of the protohalo size history can induce a strong halo assembly bias effect for massive halos. This effect is detectable in observation using the central-to-total stellar mass ratio as a proxy of the protohalo size. The correlation to the descendant central-to-total stellar mass ratio and the halo assembly bias effect seen in the protohalo size are much stronger than that seen in the commonly adopted half-mass formation time derived from the mass accretion history. This indicates that the information loss caused by the compression of halo merger trees to mass accretion histories can be captured by the protohalo size history. Protohalo size thus provides a useful quantity to connect protoclusters across cosmic time and to link protoclusters with their descendant clusters in observations.

**Key words:** methods: statistical - galaxies: groups: general - dark matter - large-scale structure of Universe

## 1 INTRODUCTION

In the  $\Lambda$ CDM cosmological framework, cosmic structures originate from small primordial perturbations in the very early Universe. These density fluctuations are then amplified by gravity and eventually form virialized structures called dark matter halos. The evolution of cosmic structures proceeds hierarchically, where small halos form first and subsequently assemble into larger halos (White & Rees 1978; Mo et al. 2010). In this scenario, gravitational potential wells associated with dark matter halos provide conditions for the formation of galaxies, and so galaxies and halos are expected to

be tightly connected with each other. Therefore, understanding the assembly of dark matter halos is a key step towards understanding the formation and evolution of galaxies (see Baugh 2006; Mo et al. 2010; Wechsler & Tinker 2018, for reviews). Dark matter halos can be characterized from three perspectives.

The first is from the evolution of dark matter halos with cosmic time. The formation and assembly of dark matter halos can be well-described by halo merger trees (Press & Schechter 1974; Lacey & Cole 1993; Somerville & Kolatt 1999). Such a tree structure grows from the descendant halo and splits into progenitor halos backward in time recursively. Halo merger trees are informative but complex. It is therefore necessary to compress the information by extracting a small set of important features from full merger trees to describe halo assembly processes. A common practice is to focus on the main

\* Contact e-mail: wkcosmology@gmail.com

branch by recursively selecting the main progenitor. The halo mass growth along the main branch is commonly referred to as the mass accretion history (Wechsler et al. 2002; Zhao et al. 2009; Katsianis et al. 2023). A characteristic halo formation time can be defined as the highest redshift when the halo has accreted half of its final halo mass, or the redshift when the halo switches from fast accretion to slow accretion (Wechsler et al. 2002; Zhao et al. 2003a; Gao et al. 2005; Wechsler et al. 2006).

The second perspective on dark matter halos is their internal structure. Navarro et al. (1997) found that the density profile of dark matter halos can be well-described by a universal profile

$$\rho(r) = \frac{\rho_s}{(r/r_s)(1+r/r_s)^2} \quad (1)$$

where  $\rho_s$  is the density parameter and  $r_s$  is a scaling radius. The asymptotic behavior of this profile is  $\rho \propto r^{-1}$  for  $r \ll r_s$  and  $\rho \propto r^{-3}$  for  $r \gg r_s$ . In practice, a dark matter halo is restrained within a radius,  $R_{\text{vir}}$ , within which the mean density is equal to some chosen value, and the total mass within  $R_{\text{vir}}$  is defined as the halo mass,  $M_{\text{vir}}$ . Therefore, the NFW halo can be characterized with two other variables: the halo mass  $M_{\text{vir}}$  and the halo concentration  $c = R_{\text{vir}}/r_s$ . In addition, dark matter halos also exhibit non-spherical shape and the deviation from the spherical symmetry is more prominent for massive halos (Jing & Suto 2002; Allgood et al. 2006). Finally, dark matter halos also possess substructures from undissolved recent halo mergers (Moore et al. 1999; Yang et al. 2011; Jiang & van den Bosch 2016).

The last perspective on the halo population is from the spatial distribution, or the clustering of halos. The spatial distribution of dark matter halos can be characterized by the two-point correlation function and higher-order statistics. The primary feature of halo clustering is the dependence on the halo mass, where massive halos are more clustered than low-mass halos. This phenomenon can be explained with a Gaussian initial density field and the extended Press-Schechter formalism (Mo & White 1996; Sheth et al. 2001). Moreover, the clustering of dark matter halos also depends on their secondary properties, which is usually referred to as the halo assembly bias. Gao et al. (2005) first identified the dependence on halo formation time (see also Wechsler et al. 2006; Li et al. 2008; Wang et al. 2009; Mansfield & Kravtsov 2020; Wang et al. 2021b; Lazeyras et al. 2017, 2021; Barreira et al. 2021). Subsequent studies also find halo assembly bias caused by halo concentration, halo spin, and other properties (e.g. Gao & White 2007; Jing et al. 2007; Wang et al. 2011). There are also attempts to detect such effects in observations, with mixed results (e.g. Wang et al. 2013a; Zu et al. 2021; Wang et al. 2022).

A comprehensive understanding of dark matter halos requires not only knowledges from each perspective, but also relationships among properties in these three categories. In this respect, one important question is how halo structures are shaped by their assembly histories. Navarro et al. (1997) proposes a simple model that the difference in halo formation time and the time-dependence of cosmic density result in different halo concentrations. This model is further improved by subsequent studies (Bullock et al. 2001; Wechsler et al. 2002; Zhao et al. 2003a,b; Lu et al. 2006; Zhao et al. 2009; Diemer & Joyce 2019). Recently, Wang et al. (2020a) investigated the importance of merger events in shaping the halo concentration, and found that secular evolutions increase the concentration while sudden halo mergers reduce the concentration.

There is, however, one unresolved question on the relationship among halo structure, halo assembly history, and halo clustering. Jing et al. (2007) found that the halo assembly bias induced by the

halo concentration is much stronger than the halo formation time for halos above  $\gtrsim 10^{13} h^{-1} M_{\odot}$ . A detailed analysis in Mao et al. (2018) revealed that paired and unpaired cluster-size halos have nearly identical mass accretion histories, and so there is no correlation between halo clustering and halo formation time, in contrast to results obtained by Chue et al. (2018). The question is: if the halo structure is determined by its assembly history, why the assembly bias of the halo concentration is absent in the mass accretion history for cluster-size halos? One possible reason is that the assembly history alone cannot determine the structure of descendant halos (see Ludlow et al. 2012). Another explanation is that the information about the halo assembly bias is lost during the data compression from halo merger trees to mass accretion histories. Wang et al. (2021b) proposed that the halo formation time is determined by both internal and external factors, which can produce opposite halo assembly bias effects with similar amplitudes for massive halos. Therefore, the halo assembly bias effect of the halo formation time is very weak. In that case, a different compression method might be needed to retain the information about halo assembly bias.

In this study, we propose a new method to characterize the assembly of dark matter halos, using the redshift evolution of protohalo sizes. This paper is organized as follows. § 2 introduces the simulation data used in this study. § 3 presents the redshift evolution of protohalo sizes and their relation to descendant halos. § 4 shows the assembly bias effect in terms of protohalo size. Finally, the discussion and summary of our main results are presented in § 5.

## 2 DATA

In this study, we use the ELUCID simulation (Wang et al. 2013b, 2014, 2016; Tweed et al. 2017), which is a constrained N-body simulation to reconstruct the density field and formation history of our local Universe based on the Sloan Digital Sky Survey DR7 (York et al. 2000; Abazajian et al. 2009). This simulation has  $3072^3$  dark matter particles, each with a mass of  $3.09 \times 10^8 h^{-1} M_{\odot}$ , in a box with a side length of  $500 h^{-1} \text{Mpc}$ . The simulation assumes a  $\Lambda\text{CDM}$  cosmology with  $\Omega_m = 0.258$ ,  $\Omega_{\Lambda} = 0.742$ ,  $\sigma_8 = 0.80$ , and  $h = 0.72$ .

Dark matter halos are identified using the Friends-of-Friends algorithm (Davis et al. 1985), and their masses are assigned as the total dark matter mass enclosed within a radius where the mean overdensity is 200 times of the critical density. The ELUCID simulation is complete for halos to  $10^{10} h^{-1} M_{\odot}$  up to  $z \sim 8$  (Wang et al. 2016). The concentration,  $c = R_{\text{vir}}/r_s$ , of each FoF halo is estimated through their first moment, i.e.  $R_1 = \int_0^{R_{\text{vir}}} 4\pi r^3 \rho(r) dr / M_{\text{vir}} / R_{\text{vir}}$ , whose relation to the concentration of NFW halos can be expressed analytically (see Wang et al. 2024, for details). In each FoF halo, subhalos are identified with the SUBFIND algorithm (Springel et al. 2001), where the most massive subhalo is defined as the central subhalo and the remaining ones are satellite subhalos. Subhalos are linked to their progenitors and descendants using the code provided by Springel et al. (2005). The main branch of each subhalo is defined by recursively selecting the most massive progenitor. The peak mass, denoted as  $M_{\text{peak}}$ , for each subhalo is defined as the maximum halo mass that it has achieved when it is a central subhalo. Finally, a protohalo is defined as the collection of all progenitor halos at a given  $z > 0$  that would end up in a common descendant halo at  $z = 0$  (Wang et al. 2021a). Stellar masses are assigned to individual subhalos following the stellar mass-halo mass relation in `UniverseMachine` based on  $M_{\text{peak}}$  for each subhalo (see Eq. J1

in Behroozi et al. 2019). For each cluster at  $z = 0$ , we denoted its central stellar mass as  $M_{*,\text{cen}}$ , and its total stellar mass as  $M_{*,\text{tot}}$ . In this study, we use all dark matter halos above  $10^{13}h^{-1}M_{\odot}$  at  $z = 0$  and trace their progenitor halos above  $10^{10}h^{-1}M_{\odot}$  to  $z = 8$ .

### 3 THE PROTOHALO SIZE HISTORY AND ITS RELATION TO DESCENDANT HALOS

#### 3.1 Protohalo size and its redshift evolution

The assembly of a dark matter halo can be fully characterized by its merger tree. A snapshot of a halo merger tree at  $z > 0$  gives a collection of halos that will eventually end up in the halo at  $z = 0$ . Here we define this collection of halos at  $z > 0$  as a protohalo of its descendant halo at  $z = 0$  (Wang et al. 2021a). We define the size of a protohalo as

$$R = \sqrt{\frac{\sum m_i \|\mathbf{x}_i - \mathbf{x}_{\text{cen}}\|^2}{\sum m_i}}, \quad \mathbf{x}_{\text{cen}} \equiv \frac{\sum_i m_i \mathbf{x}_i}{\sum_i m_i} \quad (2)$$

where  $m_i$  and  $\mathbf{x}_i$  are the mass and comoving position of the  $i$ -th progenitor halo,  $\mathbf{x}_{\text{cen}}$  is the center of mass, and the sum is for all halos above some mass threshold. We trace all the progenitor subhalos for each descendant subhalo contained in the  $z = 0$  main halo, from which we select all central subhalos at a given redshift and use their  $M_{200c}$  as  $m_i$  to perform the summation in equation (2). For our main presentation, we choose the threshold to be  $10^{10}h^{-1}M_{\odot}$  on the basis of ELUCID resolution. In Appendix A, we show that the ranking of protohalo sizes is nearly unaffected by the choice of the mass threshold. In addition, we also show in Appendix B that using the center determined by a few dominating halos to replace  $\mathbf{x}_{\text{cen}}$  does not alter the ranking of protohalo sizes significantly.

Fig. 1 shows the spatial distribution of member halos for four protohalos with similar descendant halo mass but with different sizes at  $z \sim 2$ . The left and right two columns are two examples of protohalos with large and small sizes, respectively. The three rows show projections in three directions, and the origins are chosen to be the center of mass,  $\mathbf{x}_{\text{cen}}$ . Here the red, blue, and cyan circles represent halos with mass above  $10^{13}$ ,  $10^{12}$  and  $10^{11}h^{-1}M_{\odot}$ , respectively, and black dots are for halos in the mass range of  $10^{10} - 10^{11}h^{-1}M_{\odot}$ . Despite the fact that these protohalos will eventually collapse to form descendant halos of similar masses at  $z = 0$ , their spatial distributions at high  $z$  are very diverse: the difference in linear size between the two extremes could be as large as a factor of  $\sim 3$ . Large protohalos (the left two columns) show diverse morphologies with abundant low-mass halos, and their most massive halos are not so different from other massive member halos. In contrast, small protohalos (the right two columns) are more compact with less abundant member halos. They usually have a dominating halo, whose mass can be 10 times higher than the second one, located near the center of mass. The diversity in protohalo sizes motivates us to investigate the information on halo assembly and structure encapsulated in this quantity.

Fig. 2 shows the redshift evolution of the protohalo size of four halos selected at  $z \sim 0$  with different halo masses. First of all, the redshift evolution of protohalo size is well-behaved. It is nearly a constant above  $z \sim 2$ , below which it rapidly collapses into a virialized halo by  $z = 0$ . Most strikingly, the turnover point occurs at  $z \sim 2$  across the whole halo mass range (see also Fig. 4). Secondly, the protohalo size above  $z \sim 2$  monotonically increases with the descendant halo mass. And the protohalo size is  $\sim 2\text{Mpc}$  for group-size halos,  $\sim 5\text{Mpc}$  for ‘‘Fornax’’-like halos,  $\sim 6\text{Mpc}$  for

‘‘Virgo’’-like halos, and  $\gtrsim 10\text{Mpc}$  for ‘‘Coma’’-like halos. The correlation between protohalo size and the descendant halo mass is expected, because the formation of a more massive halo requires matter distributed over a larger volume at high  $z$  due to the homogeneity of the early Universe. Finally, the redshift evolution of protohalo size is rather smooth.

Fig. 2 also shows the mass accretion history, which is the halo mass evolution on the main branch, in magenta circles. The halo mass difference between current halos and their main progenitors at  $z \sim 8$  is up to 3-5 dex, indicating that the mass accretion history based on the main branch only captures a small portion of the whole protohalo at high  $z$ . The dashed vertical line in each panel shows the half-mass redshift when the main progenitor has achieved half of its final halo mass. The small values of the half-mass redshift indicate that they only characterize the late-time evolution of halos.

The protohalo size history and the mass accretion history are two ways to compress the halo merger tree into a one-dimensional function, and further compression may be achieved by fitting these histories with some simple parametric forms. Motivated by the two-stage evolution of protohalo size observed above, we use a double power-law function to fit its evolution from  $z \sim 8$  to  $z \sim 0$ :

$$R(z) = \frac{2R_c(z/z_c)^\alpha}{1 + (z/z_c)^{\alpha-\beta}} \quad (3)$$

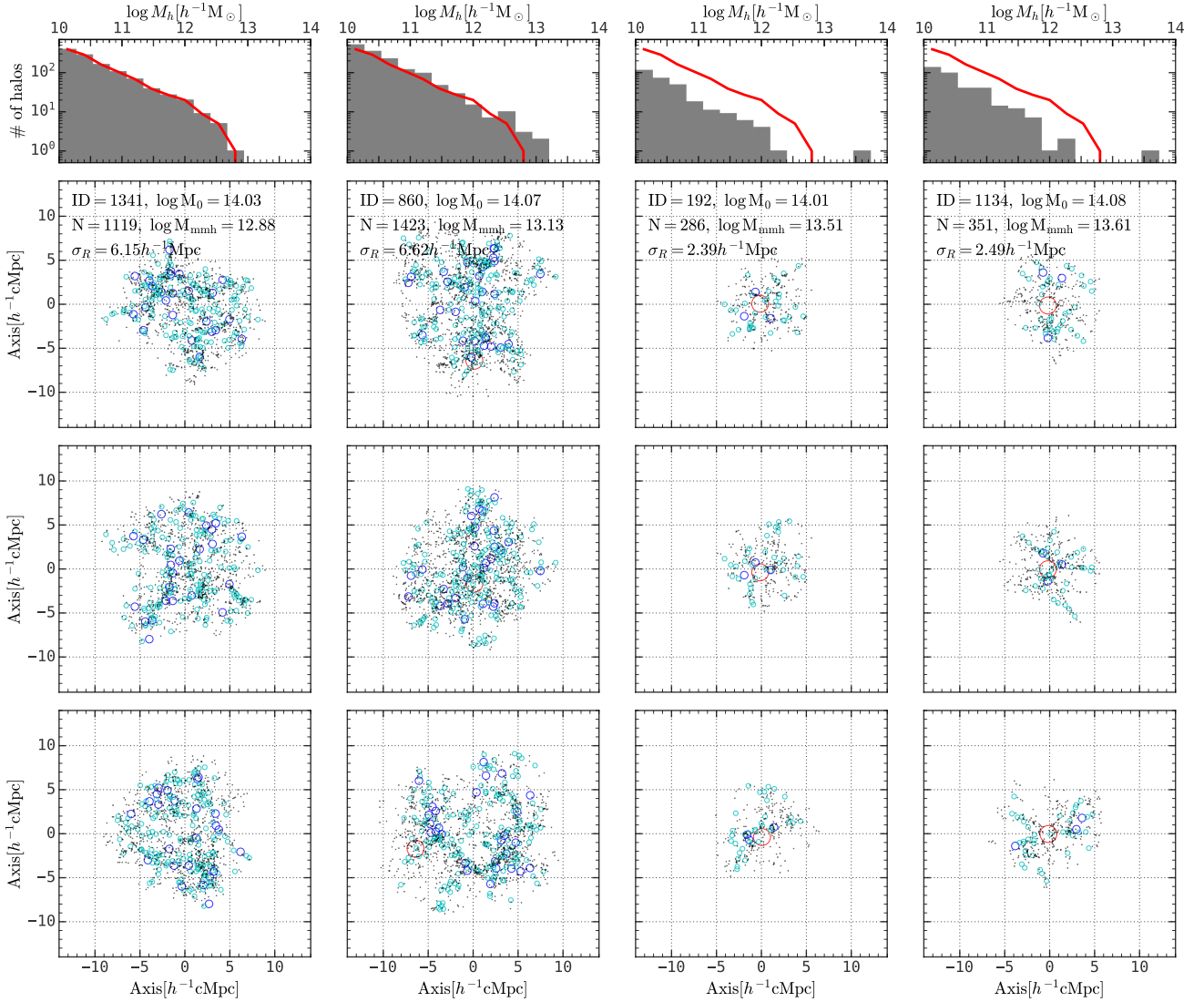
where  $R_c = R(z_c)$  is the amplitude of the protohalo size history. If  $\alpha > \beta$ , then  $R(z) \propto z^\alpha$  for  $z \ll z_c$  and  $R(z) \propto z^\beta$  for  $z \gg z_c$ . We assume prior ranges of  $\alpha \in (0, 5)$  and  $\beta \in (-1, 1)$  for  $\alpha$  and  $\beta$ , respectively, and set  $z_c = 2$  as it is sufficient to fit the data (see Fig. 2). This functional form can accurately describe individual protohalo size history across the whole halo mass range probed according to our visual inspection.

Fig. 3 shows the dependence of fitting parameters on the descendant halo mass. Here one can see that the late-time slope  $\alpha$  is around 1 and it has a marginal dependence on the descendant halo mass, with low-mass halos tending to collapse slightly more rapidly. The early-time slope  $\beta$  is independent of the descendant halo mass, and has a median value of  $-0.2$ . Finally, the amplitude  $R_c$  has a power-law relation with the descendant halo mass, with a logarithmic slope of  $\sim 0.39$ . In an ideal situation where descendant halos form from a uniform density field, we expect  $d \log R_c / d \log M_0 = 1/3 \approx 0.33$ , which is close to our result here.

#### 3.2 Relation to the structure of descendant halos

Here we first study the relation between the protohalo size history and the substructure of descendant halos. We adopt the central-to-total stellar mass ratio to characterize the substructure, for the following reasons. First of all, this quantity is observable, so that the results obtained here can be related to observations. Secondly, the stellar mass used here is obtained according to the  $M_{\text{peak}}$  of each subhalo (see § 2) and this relation is well-established at  $z \sim 0$  (Wechsler & Tinker 2018). Finally,  $M_{\text{peak}}$  is less affected by the resolution of simulations, while other quantities for substructures, such as the subhalo mass, require high resolution for reliable estimates (Jiang & van den Bosch 2016).

We find that the protohalo size history strongly correlates with the substructures of descendant halos. Fig. 4 shows the average protohalo size evolution as a function of redshift with different descendant halo masses,  $\log M_0$ , where the error bars show the median and the 16<sup>th</sup> – 84<sup>th</sup> percentiles and the solid lines are the fitting results of the double power-law function. In each bottom panel,



**Figure 1.** The member halo spatial distribution for four example protohalos at  $z \sim 2$  with descendant halo mass around  $10^{14} h^{-1} M_{\odot}$ . The left two columns are two examples with large protohalo sizes, and the right two columns are two examples with small protohalo sizes. The top panels show the halo mass distribution in each protohalo, and the halo mass distribution of the leftmost protohalo is overplotted on each panel in red solid curves for reference. The bottom three rows are for different projection directions. Halos above  $10^{13}$ ,  $10^{12}$ , and  $10^{11} h^{-1} M_{\odot}$  are shown in red, blue, and cyan circles, and halos within  $10^{10} - 10^{11} h^{-1} M_{\odot}$  are shown in black dots. The information about each halo, including the ID in ELUCID, the descendant halo mass, the richness, the halo mass of the most massive halo, the protohalo size, is shown in each row. This figure demonstrates the large diversity of spatial distribution of protohalos at given descendant halo mass.

descendant halos are further divided into four subsamples according to their central-to-total stellar mass ratios,  $\log M_{*,\text{cen}}/M_{*,\text{tot}}$ , where the stellar mass is assigned using the empirical relations in `UniverseMachine`. At  $z > 2$ , the amplitude of the protohalo size history has a strong dependence on the central-to-total stellar mass ratio of descendant halos, where halos with higher  $\log M_{*,\text{cen}}/M_{*,\text{tot}}$  tend to have smaller protohalos. Quantitatively, the difference in the protohalo size for halos with the top-10% and bottom-10% central-to-total stellar mass ratios is about 0.2-0.3 dex, despite that the  $1 - \sigma$  range of the protohalo size in each descendant halo mass bin is only  $\sim 0.1$ -0.2 dex (see top panels).

A quantitative correlation analysis is presented in Fig. 5, which shows the relation between the parameters in equation 3 and the

central-to-total stellar mass ratio,  $\log M_{*,\text{cen}}/M_{*,\text{tot}}$ , of descendant halos in four narrow halo mass bins. The top panels show the results for the late-time slope  $\alpha$ , where Spearman's rank correlation coefficient is about 0.5 across the whole halo mass range. Descendant halos with more dominating central galaxies tend to have steeper late-time slopes, indicating more rapid collapses of protohalos to form descendant halos. The panels in the middle row show results for the early-time slope  $\beta$ , whose correlation with  $\log M_{*,\text{cen}}/M_{*,\text{tot}}$  is negligible. Finally, the bottom panels show results for the amplitude of the protohalo size history,  $\log R_c$ , where Spearman's rank correlation coefficient is about 0.8. The difference in  $\log R_c$  for halos with the highest and lowest  $\log M_{*,\text{cen}}/M_{*,\text{tot}}$  is about 0.4 dex, compared to the  $1 - \sigma$  width of  $\log R_c$  in each halo mass bin, which

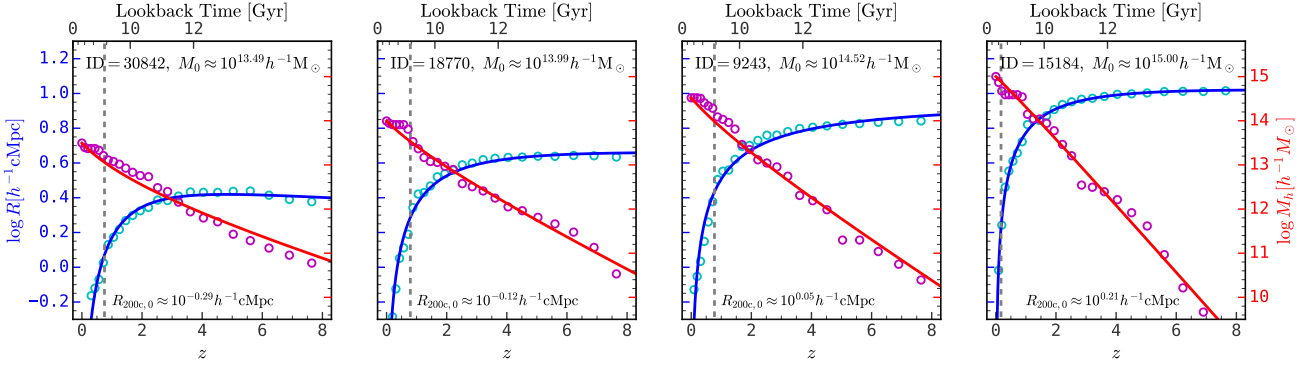


**Figure 2.** The protohalo size histories (cyan circles and blue solid lines on the left y-axis) and the mass accretion histories (magenta circles and red solid lines on the right y-axis) for four halos selected at  $z \sim 0$ . The circles are the histories calculated from each snapshot, and the solid lines are the fitting functions from equations 3 and 5. The vertical dashed lines show the half-mass time  $z_{\text{half}}$  for each halo.

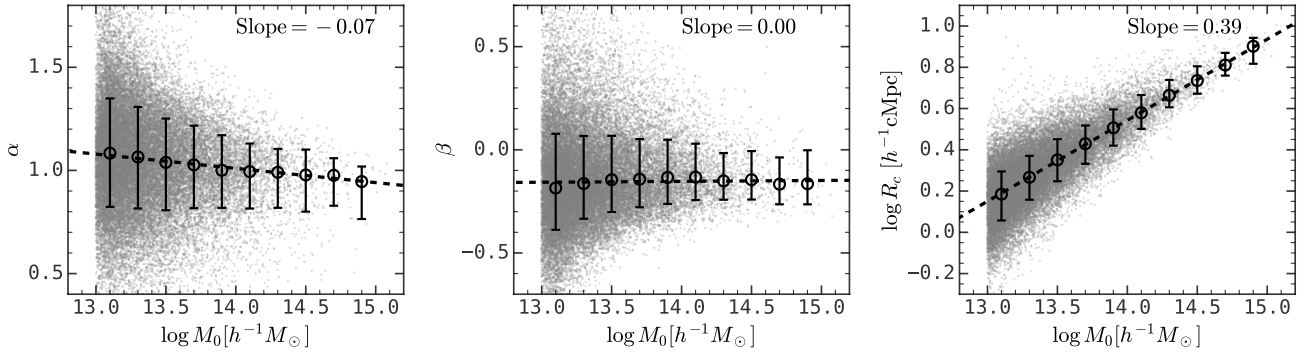


**Figure 3.** The scatter of the descendant halo mass and three parameters for the protohalo size histories in equation 3. The error bars show the median and the 16<sup>th</sup> – 84<sup>th</sup> percentiles. The black dashed lines are the linear fitting functions to the median values, where the slope is labeled on each panel.

is about 0.1-0.2 dex (see the top panels of Fig. 4). In addition, we find that the dependence of  $\log R_c$  on  $\log M_0$  and  $\log M_{*,\text{cen}}/M_{*,\text{tot}}$  can be described concisely by

$$\log \frac{R_c}{h^{-1} \text{Mpc}} = a_1 \times \log \frac{M_{*,\text{cen}}}{M_{*,\text{tot}}} + a_2 \quad (4)$$

$$a_1 = 0.31 \times \log \frac{M_0}{h^{-1} M_\odot} - 4.80$$

$$a_2 = 0.28 \times \log \frac{M_0}{h^{-1} M_\odot} - 3.55$$

As one can see from Fig. 6, the predicted  $\log R_c$  matches the true  $\log R_c$  well and the width for the 16<sup>th</sup> – 84<sup>th</sup> percentiles is smaller than 0.1 dex.

In Appendix C, we restrained the protohalo as the collection of halos that will end up in descendant subhalos within the virial radius of the descendant main halo. This will effectively eliminate member halos on the protohalo outskirts, since they are likely to become subhalo outside the descendants' virial radius. We found that the correlation between the protohalo size and the central-to-total stellar mass ratio is compromised but still as high as  $\approx 0.6$ .

In Appendix D, we perform a similar analysis using the IllustrisTNG simulation (Pillepich et al. 2018a) and obtain similar results to Figs. 4 and 5, which indicates that the results obtained

here do not depend on the specific stellar mass-halo mass relation in UniverseMachine.

The relation between  $\log R_c$  and  $\log M_{*,\text{cen}}/M_{*,\text{tot}}$  can be explained qualitatively. To begin with, the total mass in the region occupied by a protohalo is proportional to its final descendant halo mass. At a given descendant halo mass, protohalos with larger sizes collapse at later times due to their relatively shallow gravitational potential. Therefore, the halo-halo merger events occur relatively late, and it becomes less probable for these late-accreted satellite subhalos and their galaxies to be cannibalized by their central subhalos and central galaxies. Consequently, these systems have more substructures, which results in low values of  $\log M_{*,\text{cen}}/M_{*,\text{tot}}$ .

Finally, Fig. 7 shows a moderate negative correlation between  $\log R_c$  and the halo concentration,  $c$ , where high-concentration halos have more compact protohalos. The rank correlation coefficient is  $\geq 0.5$  for group-size halos and decreases to 0.3 for cluster-size halos. This result is consistent with the result in Wang et al. (2021b), where it was found that high-concentration halos have higher overdensity in Lagrangian space.

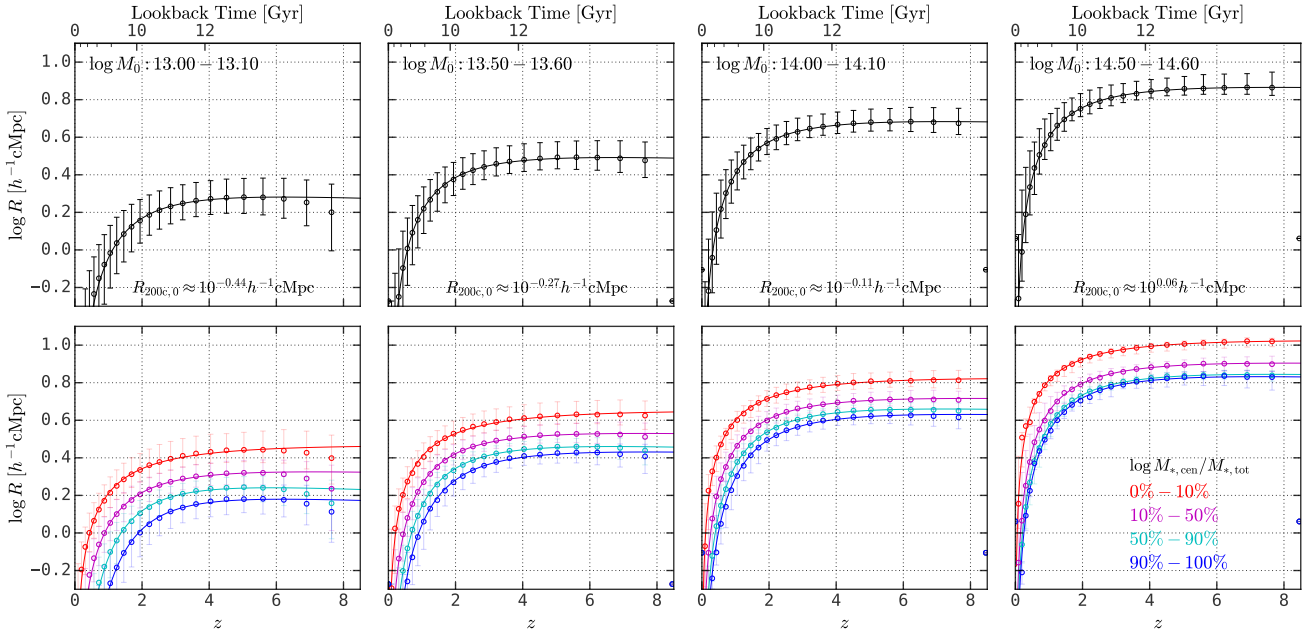


**Figure 4.** Top panels: The redshift evolution of protohalo size,  $R$ , in four halo mass bins. Bottom panels: In each halo mass bin, halos are divided into four equal-size subsamples according to their  $\log M_{*,\text{cen}}/M_{*,\text{tot}}$ . The error bars show the median and the 16<sup>th</sup> – 84<sup>th</sup> percentiles. This figure demonstrates the strong correlation between the protohalo size history and the  $\log M_{*,\text{cen}}/M_{*,\text{tot}}$  of descendant halos.

### 3.3 Relation to the mass accretion history

The hierarchical formation process of dark matter halos can be fully characterized by halo merger trees. However, these tree-like structures are too complicated to use directly in the modeling of halo assembly. Some data compression is required. There have been attempts to extract compressed information from halo merger trees. A common method is to compress the halo merger tree into the mass accretion history (Wechsler et al. 2002; Zhao et al. 2003a). Further data compression can be done by defining some characteristic formation time, fitting the mass accretion history with some simple parametric forms, or using the principle component analysis technique (Wechsler et al. 2002; Gao et al. 2005; Wechsler et al. 2006; Li et al. 2008; Chen et al. 2020). Here we fit the mass accretion history with the functional form in McBride et al. (2009), which is

$$M(z) = M_0(1+z)^\gamma e^{-\delta z} \quad (5)$$

where  $M_0$  is the descendant halo mass at  $z = 0$ , and  $\gamma$  and  $\delta$  are two free parameters. McBride et al. (2009) found that the combination,  $\gamma - \delta$ , to be a useful parameter to characterize the mass accretion rate at low  $z$ , since

$$\frac{d \ln M(z)}{d \ln(1+z)} = \gamma - \delta(1+z) \approx \gamma - \delta + \mathcal{O}(z) \quad (6)$$

when  $z$  is close to zero. As shown in Fig. 2, this functional form can describe the simulated mass accretion histories reasonably well, but not in detail. One can use the fitting parameters to describe the overall properties of a mass accretion history, as we will do here. In principle, the fitting results can also be used to define a half-mass time as the highest  $z$  when the main progenitor has reached half of the final halo mass. The half-mass time defined in this way is not identical to  $z_{\text{half}}$  obtained directly from the simulation data. We have checked that both definitions give similar results, and we will use the  $z_{\text{half}}$  obtained directly from the data in our presentation.

We note that there are other attempts to compress halo merger trees using state-of-the-art statistical tools (e.g. Forero-Romero 2009; Obreschkow et al. 2020).

Our study proposes a new method which compresses a halo merger tree into a linear protohalo size history, and identifies that the most important quantity is the amplitude,  $\log R_c$ . We emphasize that the protohalo size history is correlated with the mass accretion history, but encapsulates additional information of halo assembly that is missed in the mass accretion history. As shown in Fig. 8, the amplitude of the protohalo size history,  $\log R_c$ , moderately correlates with the halo mass assembly time,  $z_{\text{half}}$ , in the sense that smaller protohalos tend to form earlier. This is expected: at fixed descendant halo mass, smaller protohalos have deeper gravitational potential well, so that the member halos can merge with each other in a shorter time scale. Fig. 8 also shows that  $\log R_c$  is in moderate correlation with  $\gamma - \delta$ , which approximates the recent mass accretion rate (see equation 6), in the sense that larger protohalos tend to experience more rapid accretion at late times. We have also looked into other features extracted from the mass accretion history and found that  $z_{\text{half}}$  exhibits the strongest correlation with  $\log R_c$ .

The protohalo size history also encapsulates information on halo assembly that is missed in the mass accretion history. First of all, as one can see from Fig. 5,  $\log R_c$  strongly correlates with the substructure of descendant halos, while a similar analysis in Appendix E shows that the correlation between the mass accretion history and the substructure of descendant halos is much weaker. Secondly,  $\log R_c$  contains extra information about the halo concentration,  $c$ . To demonstrate it, we take the residual of  $\log R_c$  and  $c$  conditioned on  $z_{\text{half}}$  and plot their relation in Fig. 9. Here one can see that these two residual quantities are still moderately correlated, with Spearman’s coefficient about 0.3. The last manifestation is in the halo assembly bias effect, as we will show in § 4.

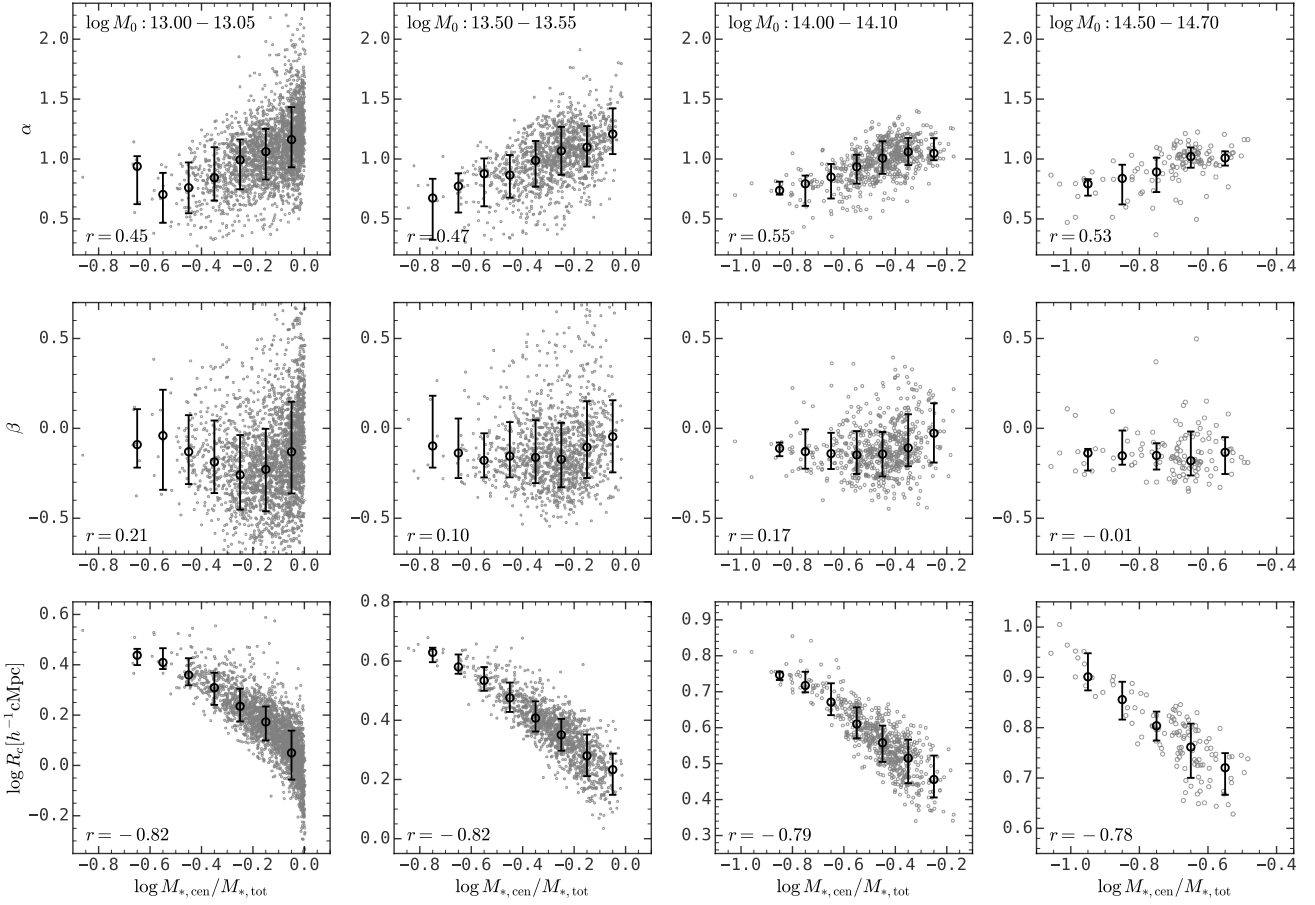


**Figure 5.** The correlation between the central-to-total stellar mass ratio,  $\log M_{*,\text{cen}}/M_{*,\text{tot}}$ , and the parameters in equation 3. Four columns are for different descendant halo mass bins, and the bin sizes are adjusted to be minimized while containing sufficient data points for statistical analysis. The top panels are for the late-time slope  $\alpha$ , the middle panels are for the early-time slope  $\beta$ , and the bottom panels are for the amplitude  $\log R_c$ . This figure demonstrates that the amplitude of the protohalo size history strongly correlates to the descendant central-to-total stellar mass ratio, as the correlation for the other two parameters is much weaker.

Finally, it is noteworthy that the mass accretion history and the protohalo size history captures different stages of halo assembly. The mass accretion history primarily features the late-time evolution when a dominant progenitor halo emerges, since the characteristic halo formation times derived from the mass accretion history, such as the half-mass time and the time when the halo transits from fast accretion to slow accretion, are below  $z \lesssim 2$  for halos above  $10^{13} h^{-1} M_\odot$ . On the contrary, the protohalo size history features the early-time evolution prior to the collapse of the protohalo, which occurs at  $z \sim 2$ . Therefore, the combination of these two quantities might give us a more complete picture of halo assembly.

#### 4 HALO ASSEMBLY BIAS

Dark matter halos are biased tracers of the underlying density field, and the square root of the ratio between the clustering strength of halos and the underlying density field is defined as the halo bias. The halo bias primarily depends on halo mass, where massive halos are more clustered (Mo & White 1996). In addition, the clustering of dark matter halos also depends on their secondary properties, including shape, formation time, concentration, and spin. Such de-

pendence is referred to collectively as the halo assembly bias (e.g. Sheth et al. 2001; Gao et al. 2005; Wechsler et al. 2006; Jing et al. 2007; Li et al. 2008; Mao et al. 2018). The existence of halo assembly bias implies the entanglement of secondary halo properties and their large-scale environments, and so an analysis of the halo assembly bias can help us better understand the formation of dark matter halos.

Here we study the assembly bias using the auto-correlation function estimated with

$$\xi(r) = \frac{DD(r)}{RR(r)} - 1 \quad (7)$$

where  $DD(r)$  is the pair counts within a distance of  $r \pm \delta r$  for the target sample, and  $RR(r)$  is the pair counts within the same distance for the random sample. We find a strong halo assembly bias effect caused by the amplitude of the protohalo size history,  $\log R_c$ . As shown in Fig. 10, the auto-correlation function is higher for halos with larger  $R_c$  compared with halos with smaller  $R_c$ . Here the subsamples with large and small protohalos are constructed based on their  $\log R_c$  relative to the median relation shown in the right panel of Fig. 3. Their descendant halo mass distributions are nearly identical, as shown in the top panels. Their auto-correlation

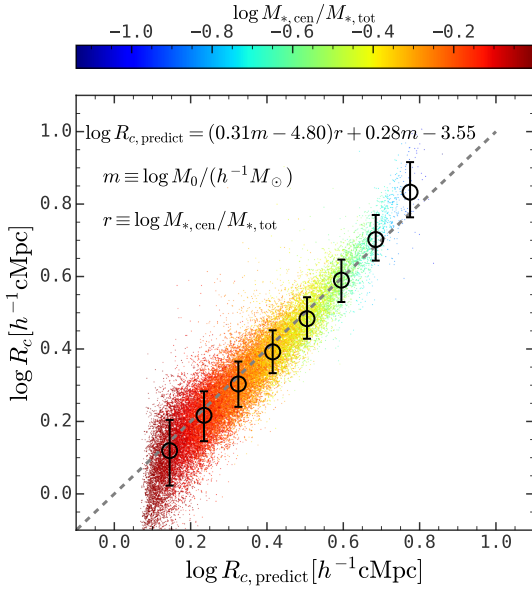


**Figure 6.** Accuracy of the amplitude of the protohalo size history, i.e.  $\log R_c$ , calibrated in equation 4. The x-axis is the prediction from the relation shown in the figure, and the y-axis is the true  $\log R_c$  for each individual halo. The color encodes the central-to-total stellar mass ratio. The error bars show the median and the 16<sup>th</sup> – 84<sup>th</sup> percentiles. This figure shows that the  $\log R_c$  calibrated against  $\log M_0$  and  $\log M_{*,cen}/M_{*,tot}$  matches the true  $\log R_c$  quite well.

functions are presented in the middle panels of Fig. 10, where the red and blue error bars are the results for large and small protohalos, respectively, and the gray shaded regions are the results for all the halos in the same mass bin. The error bars in the bottom panels show the ratio between each subsample and the parent sample. The shaded regions show the mean ratio by averaging the ratios from 10 to 30  $h^{-1}$ Mpc, which is an estimate of the square of the relative bias ( $b^2 = \xi_{\text{subsample}}/\xi_{\text{parent}}$ ). Here one can see that the bias factor between the 50% of halos with the largest  $R_c$  and the 50% with the smallest  $R_c$  is about  $\sqrt{1.2/0.8} - 1 \approx 22\%$ , which is larger than the assembly bias caused by the half-mass time. According to the results obtained in Jing et al. (2007), the bias factor of the 20% of halos with the smallest  $z_{\text{half}}$  is just about 10% larger than that the 20% with the largest  $z_{\text{half}}$ , as is also shown in Appendix E. Note that the halo assembly bias reported here extends to  $\gtrsim 40$ Mpc, although the error bars are large due to the limited simulation box size.

Like the mass accretion history, the protocluster size history is not directly observable. However, as shown in § 3.2, the central-to-total stellar mass ratio,  $\log M_{*,cen}/M_{*,tot}$ , is tightly correlated with  $R_c$ , and so can be served as an observational proxy. As a proof of concept, Fig. 11 shows the halo assembly bias manifested by  $\log M_{*,cen}/M_{*,tot}$ . Here the results are similar to the results we obtained using  $R_c$  in Fig. 10, indicating that the proxy is reliable.

Actually, halo assembly bias effects based on quantities like  $M_{*,cen}/M_{*,tot}$  have already been detected in observations. Zu et al. (2021) used the REDMAPPER cluster catalog constructed from the SDSS DR8 to study the dependence of the halo assembly bias caused by the central stellar mass to halo mass ratio, where the halo mass is controlled using the weak gravitational lensing technique. They found that the large-scale bias for clusters with lower central stellar mass is 10% higher than that of higher central stellar mass

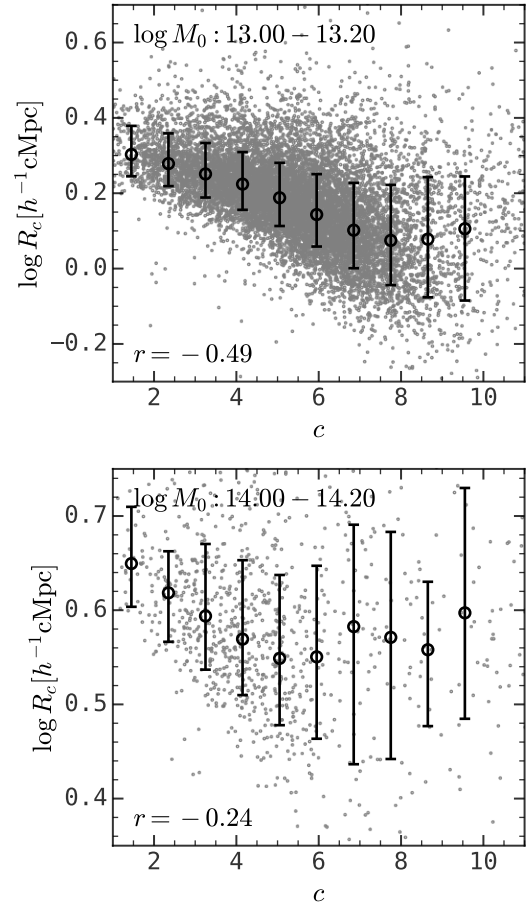


**Figure 7.** Relation between the amplitude of the protohalo size history,  $\log R_c$ , and the halo concentration,  $c$ , in two halo mass bins. The error bars show the median and the 16<sup>th</sup> – 84<sup>th</sup> percentiles. This figure shows that  $\log R_c$  negatively correlates to  $c$ .

from both weak gravitational lensing and galaxy clustering results (Zu et al. 2022). Under the assumption that the relation between total stellar mass and halo mass of these clusters is sufficiently tight (Bradshaw et al. 2020), their detection is similar to the halo assembly bias effect exhibited by the amplitude of the protohalo size history approximated by the central-to-total stellar mass ratio. Moreover, they also found a difference in the halo concentration between subsamples with large and small central stellar masses, indicating that the halo assembly bias exhibited by the protohalo size and by the halo concentration are related to each other, as shown in Fig. 7.

Finally, we note that the halo assembly bias effect is a manifestation of the entanglement between halo properties and the large-scale environment. Such effect is present for the halo concentration,  $c = R_{\text{vir}}/r_s$ , but not for the half-mass time,  $z_{\text{half}}$  (Jing et al. 2007; Wang et al. 2021b), nor the entire mass accretion history (see Mao et al. 2018, and Appendix F). This makes us wonder how the halo concentration “knows” the large-scale environment without the assembly history “knowing” it. In this study, we find that the protohalo size history exhibits a strong halo assembly bias effect. Besides, Appendix F further demonstrates that paired and un-paired cluster-size halos have nearly identical mass accretion histories, but different protohalo size histories, which suggests that the environ-



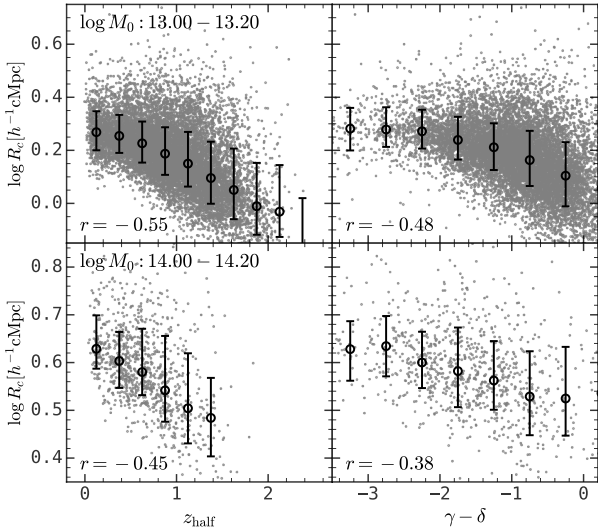


**Figure 8.** The relation between the amplitude of the protohalo size history,  $\log R_c$ , and characteristic features of massive accretion history, including the half-mass time,  $z_{\text{half}}$ , and the recent halo accretion rate,  $\gamma - \delta$ , (see equation 6). The error bars show the median and 16<sup>th</sup> – 84<sup>th</sup> percentiles. This figure shows that the halos with large protohalo sizes tend to form later and experience more rapid accretion than the halos with small protohalo size.

mental effects on halo formation must have been lost during the data compression from halo merger trees to mass accretion histories, and such effects are captured by the protohalo size history.

## 5 DISCUSSION AND SUMMARY

### 5.1 Implications for connecting protoclusters and clusters

A protocluster, by definition, is a set of dark matter halos, as well as their associated baryons, at  $z > 0$  that will eventually collapse into a common cluster-size dark matter halo at  $z = 0$ . In other words, protoclusters are protohalos whose descendant halo mass is  $\geq 10^{14} h^{-1} M_{\odot}$ . Such objects are well-defined in simulations where we can track their evolution. However, it is non-trivial to identify protoclusters in observation due to the difficulty in predicting the fate of those high- $z$  objects. A feasible way is to characterize true protoclusters in simulations with a few features, such as the galaxy number overdensity, and find objects in the observation that exhibit similar properties (e.g. Chiang et al. 2013). This kind of method is straightforward but their performance is difficult to assess since they rely on the visual inspection. A more advanced way is to develop an automatic structure finding algorithm, which can be trained in simulations and applied to mock surveys for performance assessments (e.g. Stark et al. 2015; Wang et al. 2021a).

How to build a reliable connection between protoclusters and present-day clusters is, therefore, an essential step in understanding the formation of clusters, and the evolution of cluster galaxies. Conventionally, such connections are built using masses of protoclusters and descendant clusters. For each identified protocluster, the mass can be estimated according to proxies such as the number overdensity of tracers and the total mass within the protocluster. However, the mass alone cannot capture the diversity of protocluster, as shown in Fig. 1 (see also Lovell et al. 2018).

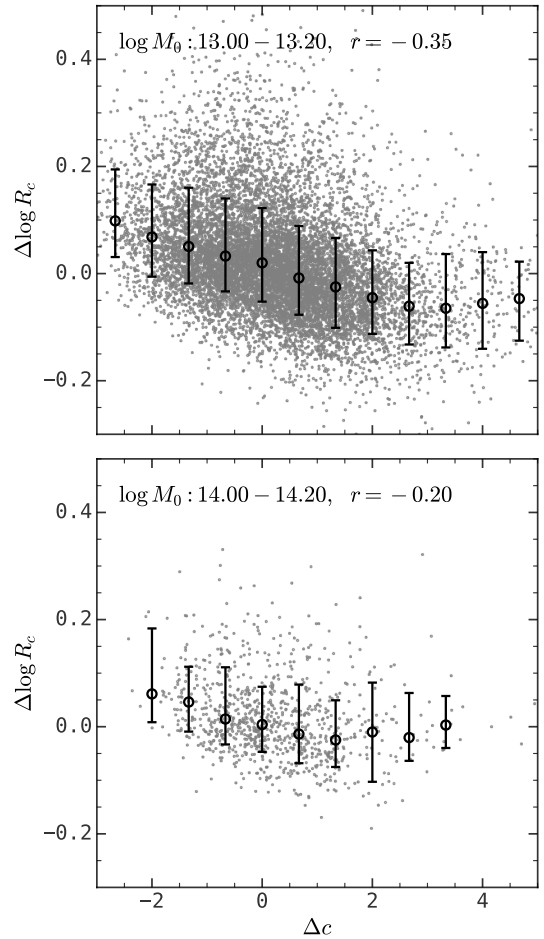


**Figure 9.** The correlation between  $\Delta c$  and  $\Delta \log R_c$  in two narrow halo mass bins. Here  $\Delta c$  and  $\Delta \log R_c$  are the difference between these two quantities and their median relation with respect to  $z_{\text{half}}$ . The error bars show the median and 16<sup>th</sup> – 84<sup>th</sup> percentiles. This figure demonstrates that the amplitude of the protohalo size history contains extra information about the descendant halo structure that is missed by the half-mass time.

We find that the protocluster size, which is defined in the same manner as the protohalo size, is an excellent secondary property to connect protoclusters across cosmic time and their descendant clusters at  $z \sim 0$ . The left and middle panels of Fig. 12 show the correlation between the central-to-total stellar mass ratio of descendant clusters and the protocluster size at  $z \sim 2$  and  $z \sim 8$ , respectively. Here one can see that these correlations are tight, with Pearson’s correlation coefficients as high as  $\sim 0.86(0.77)$  for  $z \sim 2(8)$ . The right panel shows the correlation between the sizes of protoclusters at  $z \sim 2$  and  $z \sim 8$ , and the correlation coefficient is about 0.9.

Thus, the protocluster size can be used to refine the connections of protoclusters across cosmic time and to local galaxy clusters. This refinement may be referred to as the secondary cluster-protocluster connection. Observationally, the usefulness of this refinement relies on the fact that the protocluster size and the central-to-total stellar mass ratio of descendant halos are tightly correlated and that galaxy groups and protoclusters can be reliably identified from observations (Yang et al. 2007; Wang et al. 2020b; Yang et al. 2021; Li et al. 2022). However, our findings also pose a challenge

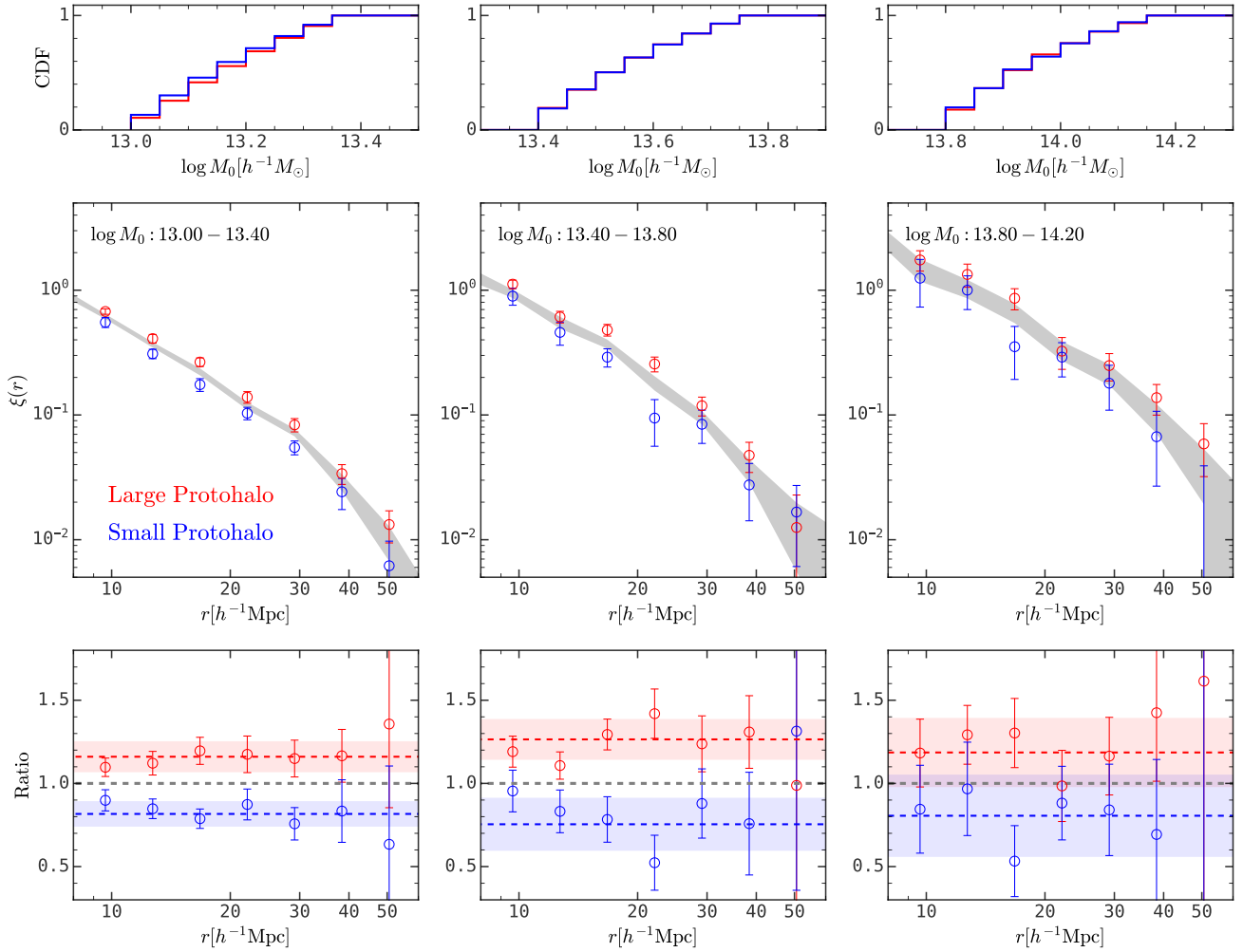


**Figure 10.** Top panels: The auto-correlation functions for dark matter halos in three halo mass bins. The gray shaded regions are for all halos in each halo mass bin. The red and blue error bars are for subsamples with  $\Delta A$  above and below zero, respectively. Bottom panels: The ratio of the auto-correlation functions between two subsamples and the parent sample in each halo mass bin. The shaded regions show the average ratio from 10 to 30  $h^{-1}$  Mpc for each subsample. This figure shows the difference in the clustering strength for halos with large and small protohalos is about  $1.2/0.8 - 1 \approx 50\%$ .

to the identification of protoclusters from observation. As we have shown, the size difference between protoclusters of similar descendant mass can be as high as  $\sim 0.5$  dex. This corresponds to a factor of  $10^{0.5 \times 3} \approx 30$  in volume, and suggests that protocluster finders based on overdensities within a fixed aperture may produce a biased protocluster catalog. Clearly, for a density-based protocluster finder, such bias needs to be quantified using realistic mock catalogs (Stark et al. 2015; Wang et al. 2021a).

## 5.2 Summary

We propose a novel method to characterize the assembly of massive dark matter halos using the protohalo size history. Our main findings are summarized as follows:

(i) The protohalo size history exhibits two-stage evolution: an early-time static phase and a late-time collapsing phase. These features can be captured by a double power-law function with a characteristic redshift at  $z = 2$  in the halo mass range between  $10^{13} h^{-1} M_{\odot}$

and  $10^{15} h^{-1} M_{\odot}$ . The late-time slope  $\alpha$  and the early-time slope  $\beta$  are nearly independent of the descendant halo mass, while the amplitude  $\log R_c$  positively correlates with the descendant halo mass with a slope of  $\sim 0.39$  (see Figs. 2 and 3).

(ii) At a given descendant halo mass, the amplitude of the protohalo size history,  $\log R_c$ , strongly correlates to the central-to-total stellar mass ratio,  $\log M_{*,\text{cen}}/M_{*,\text{tot}}$ , of the descendant halos, with smaller protohalos evolving to descendant halos that are more dominated by central galaxies. There is also a moderate correlation between the late-time slope and  $\log M_{*,\text{cen}}/M_{*,\text{tot}}$ , in the sense that more rapid collapsing produces a more dominating central galaxy (see Fig. 4 and Appendix E).

(iii) The protohalo size history correlates with the mass accretion history, but also encapsulates critical information about halo assembly that is missed by the mass accretion history. This is reflected in its tight correlation with the central-to-total stellar mass ratio,  $\log M_{*,\text{cen}}/M_{*,\text{tot}}$ , and its correlation with halo concentration when  $z_{\text{half}}$  is fixed (see Figs. 8, 5, and 9).

(iv) The amplitude of the protohalo size exhibits a strong halo

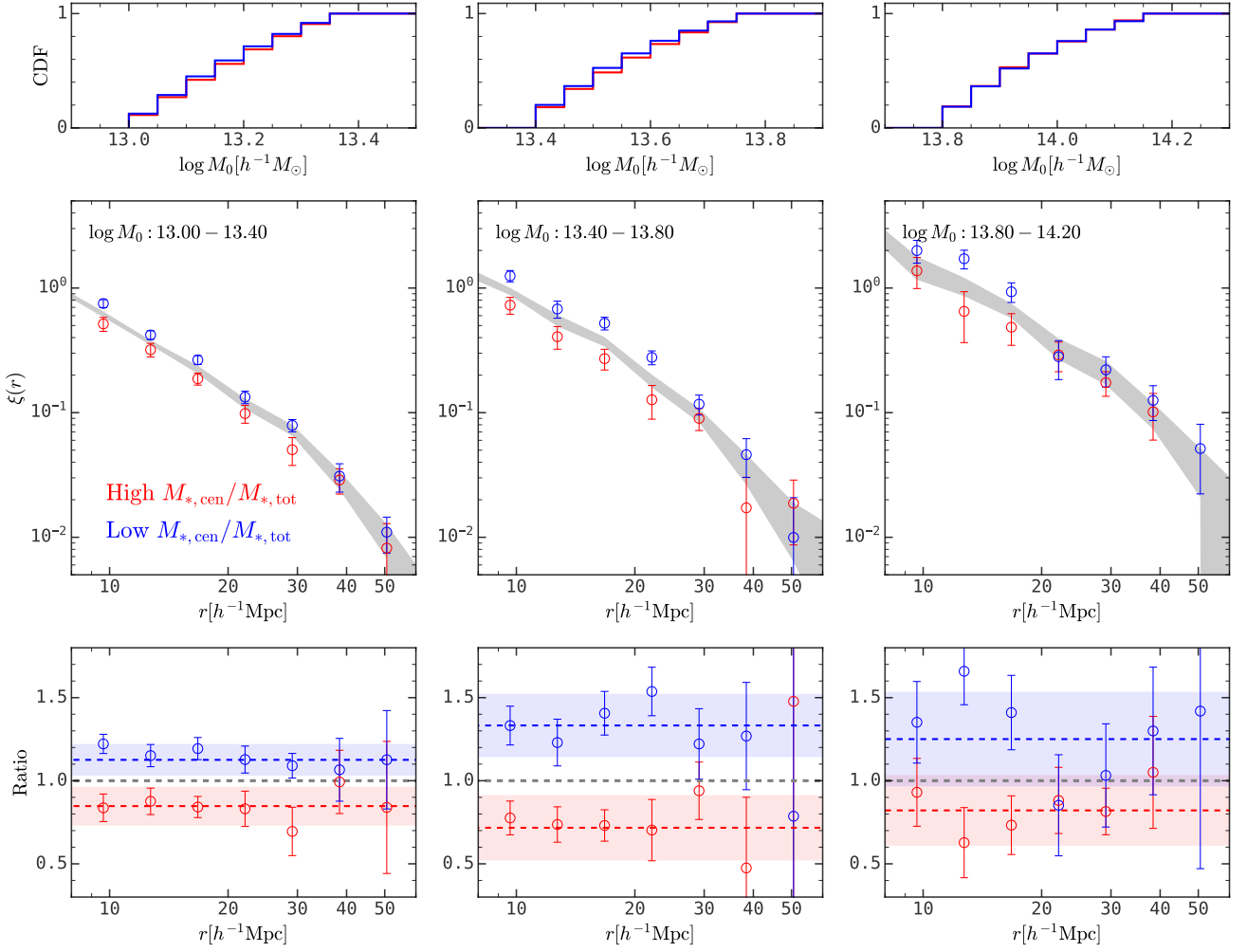


**Figure 11.** Similar to Fig. 10, except that the subsamples are divided according to their  $M_{*,\text{cen}}/M_{*,\text{tot}}$ .

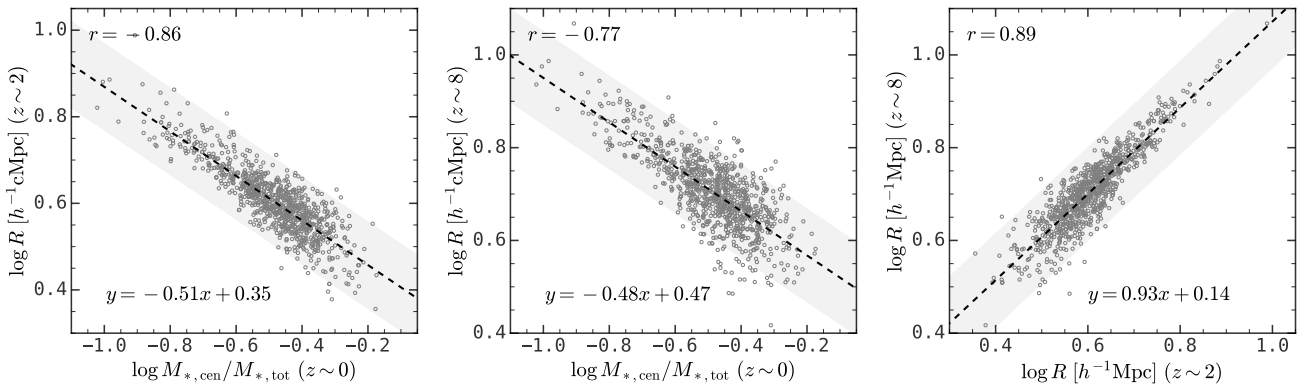


**Figure 12.** Property correlation for protoclusters at  $z \sim 2$  and  $z \sim 8$  and descendant clusters at  $z \sim 0$  with descendant halo mass between  $10^{14} h^{-1} M_{\odot}$  and  $10^{14.2} h^{-1} M_{\odot}$ . Left and middle panels: The correlation between the  $\log M_{*,\text{cen}}/M_{*,\text{tot}}$  of descendant clusters and the size of their protohalo at  $z \sim 2$  and  $z \sim 8$ , respectively. Right panel: The correlation between the sizes of protohalos at  $z \sim 2$  and  $z \sim 8$ . The black dashed lines are the linear fitting results and the shaded regions are the  $\pm 0.1$  dex regions. Pearson's correlation coefficients are presented at the top-left corner of each panel. This figure demonstrates that the protohalo size serves as an excellent secondary property to connect protoclusters across cosmic time and their descendant clusters through their  $\log M_{*,\text{cen}}/M_{*,\text{tot}}$ .

assembly bias effect, in that descendant halos of a given mass with larger protohalo sizes are more strongly correlated. A similar assembly bias effect is found for the central-to-total stellar mass ratio of descendant halos, due to its strong correlation to the protohalo size. However, the halo assembly bias exhibited by the half-mass time is much weaker at the massive end. This indicates that the information about halo assembly bias is lost during the data compression from halo merger trees to the mass accretion histories, and this information is captured by the protohalo size histories (see Figs. 10 and 11 and Appendix E).

(v) The sizes of protoclusters at  $z \sim 2$  to  $z \sim 8$  are all strongly correlated with the central-to-total stellar mass ratio of their descendant clusters at  $z \sim 0$ . The sizes of protoclusters at different redshifts are also strongly correlated to each other, which indicates the protocluster size is a useful quantity to link protoclusters at high- $z$  to their descendants at  $z \sim 0$  (see Fig. 12).

Our results suggest that the protohalo size history may provide a new avenue to study the halo assembly history and its relation to galaxy formation and evolution. The amplitude of the protohalo size history has a reliable observational proxy, which is the central-to-total stellar mass ratio. In contrast, observational proxies for the commonly-used mass accretion histories are not as reliable, especially for massive halos (Wang et al. 2023). The protohalo size history also encapsulates information about the halo assembly that is missed in the mass accretion history, as is manifested by the halo assembly bias effect. Finally, the protohalo size can be used as a secondary parameter, in addition to mass, to link protoclusters across cosmic time, and to link protoclusters to descendant clusters at  $z \sim 0$ . This will help us to better understand the assembly of galaxy clusters and the evolution of their member galaxies, when applied to the existing and upcoming high- $z$  galaxy surveys, such as MAMMOTH (Cai et al. 2016, 2017), COSMOS-Webb (Casey et al. 2022), PFS (Greene et al. 2022), and MOONS (Maiolino et al. 2020).

## ACKNOWLEDGEMENTS

The authors acknowledge the Tsinghua Astrophysics High-Performance Computing platform at Tsinghua University for providing computational and data storage resources that have contributed to the research results reported within this paper. KW and YP are supported by the National Science Foundation of China (NSFC) Grant No. 12125301, 12192220, 12192222, and the science research grants from the China Manned Space Project with NO. CMS-CSST-2021-A07. HW is supported by NSFC Grant No. 12192224.

The computation in this work is supported by the HPC toolkit **HIPP** (Chen & Wang 2023), **IPYTHON** (Perez & Granger 2007), **MATPLOTLIB** (Hunter 2007), **NUMPY** (van der Walt et al. 2011), **SCIPY** (Virtanen et al. 2020), **ASTROPY** (Astropy Collaboration et al. 2013, 2018, 2022). This research made use of NASA's Astrophysics Data System for bibliographic information.

## DATA AVAILABILITY

The data underlying this article will be shared on reasonable request to the corresponding author.

## REFERENCES

- Abazajian K. N., et al., 2009, *The Astrophysical Journal Supplement Series*, 182, 543
- Allgood B., Flores R. A., Primack J. R., Kravtsov A. V., Wechsler R. H., Faltenbacher A., Bullock J. S., 2006, *Monthly Notices of the Royal Astronomical Society*, 367, 1781
- Astropy Collaboration et al., 2013, *A&A*, 558, A33
- Astropy Collaboration et al., 2018, *AJ*, 156, 123
- Astropy Collaboration et al., 2022, *apj*, 935, 167
- Barreira A., Lazeyras T., Schmidt F., 2021, *J. Cosmology Astropart. Phys.*, 2021, 029
- Baugh C. M., 2006, *Reports on Progress in Physics*, 69, 3101
- Behroozi P., Wechsler R. H., Hearin A. P., Conroy C., 2019, *Monthly Notices of the Royal Astronomical Society*, 488, 3143
- Bradshaw C., Leauthaud A., Hearin A., Huang S., Behroozi P., 2020, *Monthly Notices of the Royal Astronomical Society*, 493, 337
- Bryan G. L., Norman M. L., 1998, *The Astrophysical Journal*, 495, 80
- Bullock J. S., Kolatt T. S., Sigad Y., Somerville R. S., Kravtsov A. V., Klypin A. A., Primack J. R., Dekel A., 2001, *Monthly Notices of the Royal Astronomical Society*, 321, 559
- Cai Z., et al., 2016, *The Astrophysical Journal*, 833, 135
- Cai Z., et al., 2017, *The Astrophysical Journal*, 839, 131
- Casey C. M., et al., 2022, *arXiv e-prints*
- Chen Y., Wang K., 2023, **HIPP**: High-Performance Package for scientific computation, Astrophysics Source Code Library, record ascl:2301.030 (ascl:2301.030)
- Chen Y., Mo H. J., Li C., Wang H., Yang X., Zhang Y., Wang K., 2020, *The Astrophysical Journal*, 899, 81
- Chiang Y.-K., Overzier R., Gebhardt K., 2013, *The Astrophysical Journal*, 779, 127
- Chue C. Y. R., Dalal N., White M., 2018, *Journal of Cosmology and Astroparticle Physics*, 2018, 012
- Davis M., Efstathiou G., Frenk C. S., White S. D. M., 1985, *The Astrophysical Journal*, 292, 371
- Diemer B., Joyce M., 2019, *The Astrophysical Journal*, 871, 168
- Forero-Romero J. E., 2009, *Monthly Notices of the Royal Astronomical Society*, 399, 762
- Gao L., White S. D. M., 2007, *Monthly Notices of the Royal Astronomical Society*, 377, L5
- Gao L., Springel V., White S. D. M., 2005, *Monthly Notices of the Royal Astronomical Society: Letters*, 363, L66
- Gao L., Navarro J. F., Cole S., Frenk C. S., White S. D. M., Springel V., Jenkins A., Neto A. F., 2008, *Monthly Notices of the Royal Astronomical Society*, 387, 536
- Greene J., Bezanson R., Ouchi M., Silverman J., the PFS Galaxy Evolution Working Group 2022, *arXiv e-prints*, p. arXiv:2206.14908
- Hunter J. D., 2007, *Computing in Science & Engineering*, 9, 90
- Jiang F., van den Bosch F. C., 2016, *Monthly Notices of the Royal Astronomical Society*, 458, 2848
- Jing Y. P., Suto Y., 2002, *The Astrophysical Journal*, 574, 538
- Jing Y. P., Suto Y., Mo H. J., 2007, *The Astrophysical Journal*, 657, 664
- Katsianis A., Yang X., Fong M., Wang J., 2023, *Monthly Notices of the Royal Astronomical Society*, 523, 1538
- Lacey C., Cole S., 1993, *Monthly Notices of the Royal Astronomical Society*, 262, 627
- Lazeyras T., Musso M., Schmidt F., 2017, *J. Cosmology Astropart. Phys.*, 2017, 059
- Lazeyras T., Barreira A., Schmidt F., 2021, *J. Cosmology Astropart. Phys.*, 2021, 063
- Li Y., Mo H. J., Gao L., 2008, *Monthly Notices of the Royal Astronomical Society*, 389, 1419
- Li Q., et al., 2022, *The Astrophysical Journal*, 933, 9
- Lovell C. C., Thomas P. A., Wilkins S. M., 2018, *Monthly Notices of the Royal Astronomical Society*, 474, 4612
- Lu Y., Mo H. J., Katz N., Weinberg M. D., 2006, *Monthly Notices of the Royal Astronomical Society*, 368, 1931
- Ludlow A. D., Navarro J. F., Li M., Angulo R. E., Boylan-Kolchin M., Bett

- P. E., 2012, *Monthly Notices of the Royal Astronomical Society*, 427, 1322
- Ludlow A. D., Bose S., Angulo R. E., Wang L., Hellwing W. A., Navarro J. F., Cole S., Frenk C. S., 2016, *Monthly Notices of the Royal Astronomical Society*, 460, 1214
- Maiolino R., et al., 2020, *Published in The Messenger* vol. 180, pp. 24–29, 6 pages
- Mansfield P., Kravtsov A. V., 2020, *Monthly Notices of the Royal Astronomical Society*, 493, 4763
- Mao Y.-Y., Zentner A. R., Wechsler R. H., 2018, *Monthly Notices of the Royal Astronomical Society*, 474, 5143
- Marinacci F., et al., 2018, *MNRAS*, 480, 5113
- McBride J., Fakhouri O., Ma C.-P., 2009, *Monthly Notices of the Royal Astronomical Society*, 398, 1858
- Mo H. J., White S. D. M., 1996, *Monthly Notices of the Royal Astronomical Society*, 282, 347
- Mo H., Van den Bosch F., White S., 2010, *Galaxy Formation and Evolution*. Cambridge University Press, Cambridge ; New York
- Moore B., Ghigna S., Governato F., Lake G., Quinn T., Stadel J., Tozzi P., 1999, *The Astrophysical Journal*, 524, L19
- Naiman J. P., et al., 2018, *MNRAS*, 477, 1206
- Navarro J. F., Frenk C. S., White S. D. M., 1997, *The Astrophysical Journal*, 490, 493
- Nelson D., et al., 2018, *MNRAS*, 475, 624
- Nelson D., et al., 2019, *Computational Astrophysics and Cosmology*, 6, 2
- Neto A. F., et al., 2007, *Monthly Notices of the Royal Astronomical Society*, 381, 1450
- Obreschkow D., Elahi P. J., Lagos C. d. P., Poulton R. J. J., Ludlow A. D., 2020, *Monthly Notices of the Royal Astronomical Society*, 493, 4551
- Perez F., Granger B. E., 2007, *Computing in Science & Engineering*, 9, 21
- Pillepich A., et al., 2018a, *MNRAS*, 473, 4077
- Pillepich A., et al., 2018b, *MNRAS*, 475, 648
- Press W. H., Schechter P., 1974, *The Astrophysical Journal*, 187, 425
- Sheth R. K., Mo H. J., Tormen G., 2001, *Monthly Notices of the Royal Astronomical Society*, 323, 1
- Somerville R. S., Kolatt T. S., 1999, *Monthly Notices of the Royal Astronomical Society*, 305, 1
- Springel V., White S. D. M., Tormen G., Kauffmann G., 2001, *Monthly Notices of the Royal Astronomical Society*, 328, 726
- Springel V., et al., 2005, *Nature*, 435, 629
- Springel V., et al., 2018, *MNRAS*, 475, 676
- Stark C. W., White M., Lee K.-G., Hennawi J. F., 2015, *Monthly Notices of the Royal Astronomical Society*, 453, 311
- Tweed D., Yang X., Wang H., Cui W., Zhang Y., Li S., Jing Y. P., Mo H. J., 2017, *The Astrophysical Journal*, 841, 55
- Virtanen P., et al., 2020, *Nature Methods*, 17, 261
- Wang H., Mo H. J., Jing Y. P., 2009, *Monthly Notices of the Royal Astronomical Society*, 396, 2249
- Wang H., Mo H. J., Jing Y. P., Yang X., Wang Y., 2011, *Monthly Notices of the Royal Astronomical Society*, 413, 1973
- Wang L., Weinmann S. M., De Lucia G., Yang X., 2013a, *Monthly Notices of the Royal Astronomical Society*, 433, 515
- Wang H., Mo H. J., Yang X., van den Bosch F. C., 2013b, *The Astrophysical Journal*, 772, 63
- Wang H., Mo H. J., Yang X., Jing Y. P., Lin W. P., 2014, *The Astrophysical Journal*, 794, 94
- Wang H., et al., 2016, *The Astrophysical Journal*, 831, 164
- Wang K., Mao Y.-Y., Zentner A. R., Lange J. U., van den Bosch F. C., Wechsler R. H., 2020a, *Monthly Notices of the Royal Astronomical Society*, 498, 4450
- Wang K., Mo H. J., Li C., Meng J., Chen Y., 2020b, *Monthly Notices of the Royal Astronomical Society*, 499, 89
- Wang K., Mo H. J., Li C., Chen Y., 2021a, *Monthly Notices of the Royal Astronomical Society*, 505, 3892
- Wang X., Wang H., Mo H. J., Shi J. J., Jing Y., 2021b, *Astronomy and Astrophysics*, 654, A67
- Wang K., Mao Y.-Y., Zentner A. R., Guo H., Lange J. U., van den Bosch F. C., Mezini L., 2022, *Monthly Notices of the Royal Astronomical Society*, 516, 4003
- Wang K., Chen Y., Li Q., Yang X., 2023, *Monthly Notices of the Royal Astronomical Society*, 522, 3188
- Wang K., Mo H. J., Chen Y., Schaye J., 2024, *Monthly Notices of the Royal Astronomical Society*, 527, 10760
- Wechsler R. H., Tinker J. L., 2018, *Annual Review of Astronomy and Astrophysics*, 56, 435
- Wechsler R. H., Bullock J. S., Primack J. R., Kravtsov A. V., Dekel A., 2002, *The Astrophysical Journal*, 568, 52
- Wechsler R. H., Zentner A. R., Bullock J. S., Kravtsov A. V., Allgood B., 2006, *The Astrophysical Journal*, 652, 71
- White S. D. M., Rees M. J., 1978, *Monthly Notices of the Royal Astronomical Society*, 183, 341
- Yang X., Mo H. J., van den Bosch F. C., Pasquali A., Li C., Barden M., 2007, *The Astrophysical Journal*, 671, 153
- Yang X., Mo H. J., Zhang Y., van den Bosch F. C., 2011, *The Astrophysical Journal*, 741, 13
- Yang X., et al., 2021, *The Astrophysical Journal*, 909, 143
- York D. G., et al., 2000, *The Astronomical Journal*, 120, 1579
- Zhao D. H., Mo H. J., Jing Y. P., Börner G., 2003a, *Monthly Notices of the Royal Astronomical Society*, 339, 12
- Zhao D. H., Jing Y. P., Mo H. J., Börner G., 2003b, *The Astrophysical Journal*, 597, L9
- Zhao D. H., Jing Y. P., Mo H. J., Börner G., 2009, *The Astrophysical Journal*, 707, 354
- Zu Y., et al., 2021, *Monthly Notices of the Royal Astronomical Society*, 505, 5117
- Zu Y., et al., 2022, *Monthly Notices of the Royal Astronomical Society*, 511, 1789
- van der Walt S., Colbert S. C., Varoquaux G., 2011, *Computing in Science & Engineering*, 13, 22

## APPENDIX A: PROTOHALO SIZES USING DIFFERENT HALO MASS LIMITS

Here we examine the impact of the halo mass limit used to estimate the protohalo size and the central-to-total stellar mass ratio of descendant halos.

The top panels of Fig. A1 show the scatter plot of the amplitude of the protohalo size history, i.e.  $\log R_c$ , estimated using progenitor halos above  $10^{10} h^{-1} M_\odot$  (the limit adopted in the main body of the paper) and  $10^{11} h^{-1} M_\odot$ , and Spearman’s rank correlation coefficients are presented in each panel. Here one can see that a higher halo mass limit will cause an underestimation of the protohalo size. This is expected since massive halos are more biased and prefer to live in central parts of protohalos. This underestimation is moderate for group-size descendant halos and negligible for cluster-size descendant halos. Most importantly, the rank correlation coefficient between different halo mass limits is  $\sim 0.96$  in the lowest descendant halo mass bin and even higher for more massive bins, indicating that such underestimation effects do not alter the relative ranks of  $\log R_c$  for these halos.

The bottom panels of Fig. A1 shows the central-to-total stellar mass ratio of descendant halos, i.e.  $\log M_{*,\text{cen}}/M_{*,\text{tot}}$ , using all subhalos with peak halo mass above  $10^{10} h^{-1} M_\odot$  and  $10^{11} h^{-1} M_\odot$ , respectively. There is nearly no difference between these two quantities, indicating again that subhalos with low peak halo mass have a negligible contribution to the total stellar mass.

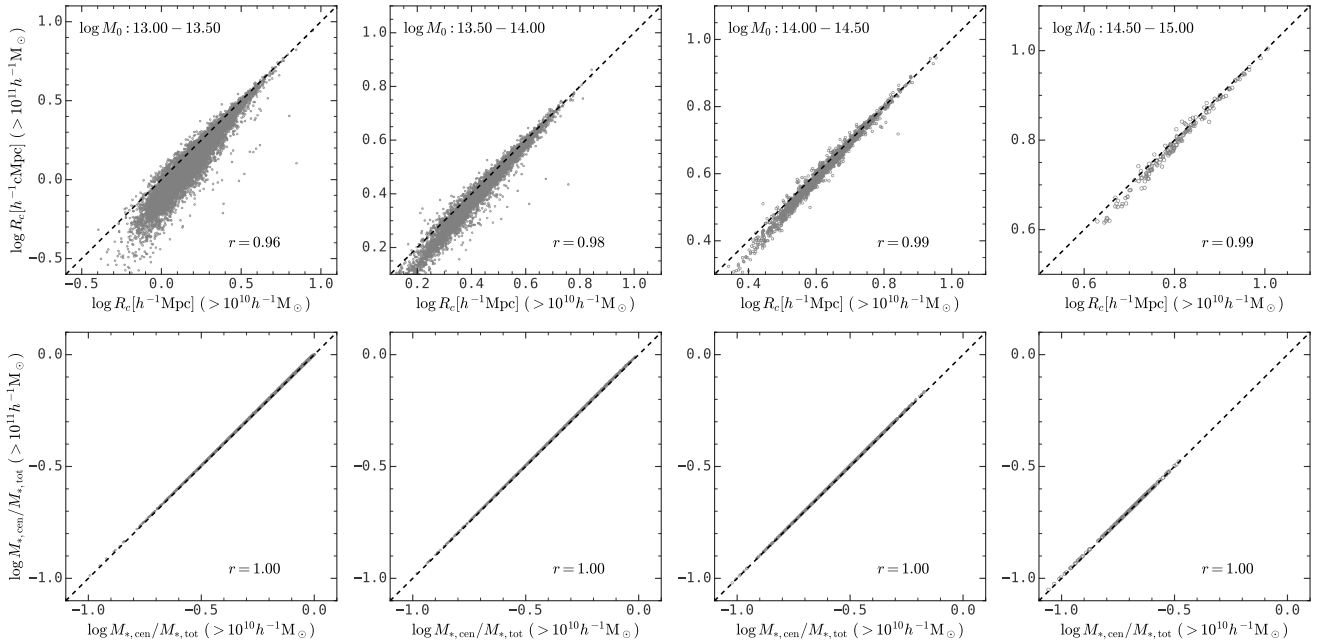


**Figure A1.** The comparison of the amplitude of the protohalo size history (top panels) and the central-to-total stellar mass ratio (bottom panels) with the halo mass limit as  $10^{10}h^{-1}M_{\odot}$  (x-axis) and  $10^{11}h^{-1}M_{\odot}$  (y-axis). Spearman’s rank correlation coefficients are presented on each panel. This figure shows that a higher halo mass limit causes an under-estimation of the amplitude of the protohalo size history,  $\log A$ , for halos with low mass and small protohalo size, but little damage to the rank of  $\log R_c$ . The impact on the central-to-total stellar mass ratio,  $\log M_{s,cen}/M_{s,tot}$  is negligible.

## APPENDIX B: PROTOHALO SIZES USING DIFFERENT CENTERING METHODS

Here we examine the impact of the protohalo centering on the protohalo size calculations. To this end, we use four different methods to determine the protohalo center  $\mathbf{x}_{cen}$ :

- (i) using the mass of center of all halos above  $10^{10}h^{-1}M_{\odot}$  in each protohalo, which is used in the main body of the paper;
- (ii) using the position of the most massive halo above  $10^{10}h^{-1}M_{\odot}$  in each protohalo;
- (iii) using the mass of center of top-2 most massive halos above  $10^{10}h^{-1}M_{\odot}$  in each protohalo;
- (iv) using the mass of center of top-3 most massive halos above  $10^{10}h^{-1}M_{\odot}$  in each protohalo.

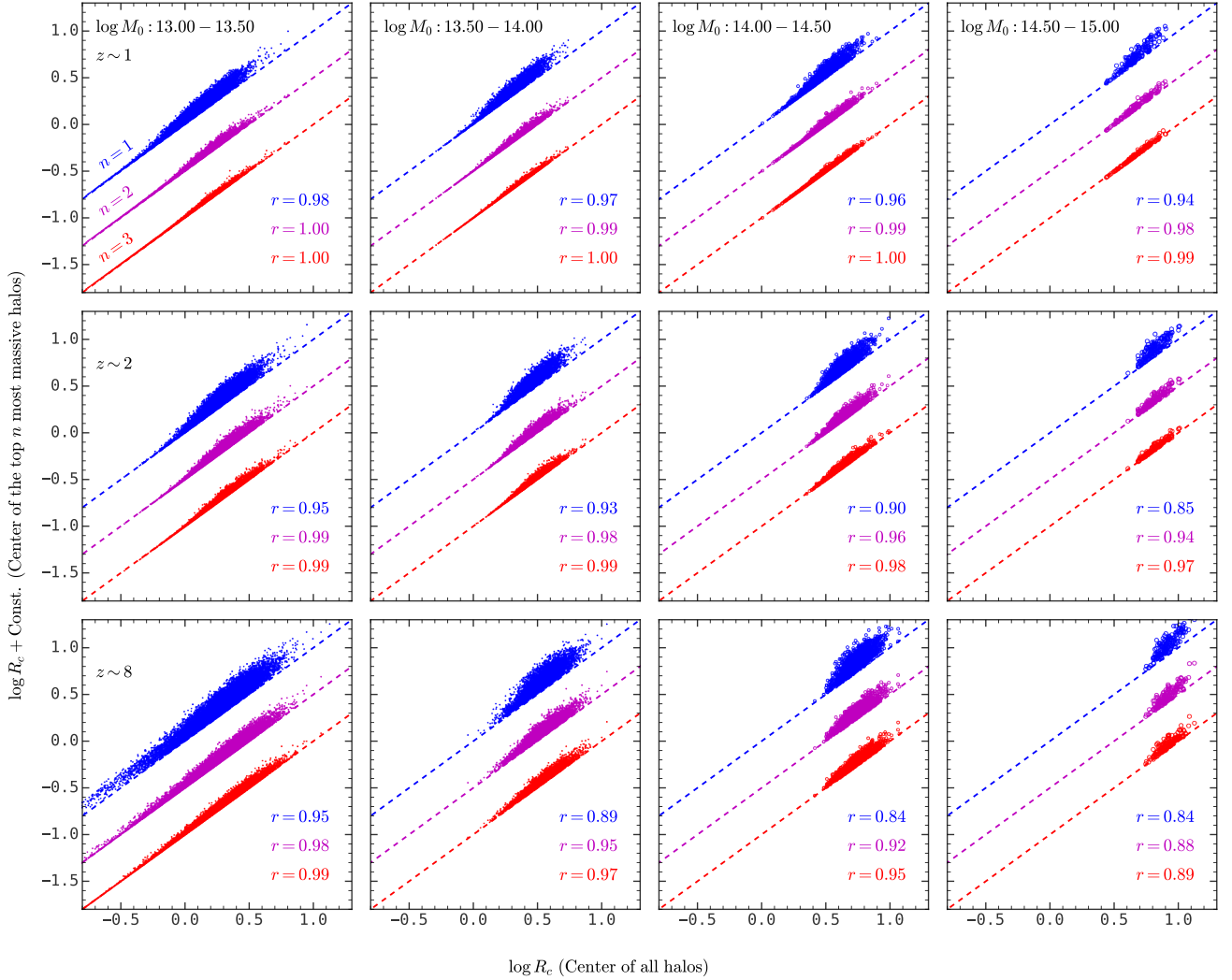
In the latter two cases, if the number of halos above  $10^{10}h^{-1}M_{\odot}$  in the protohalo is smaller than the required number, we use all the available halos.

Fig. B1 shows the scatter of the protohalo size estimated with different centering methods in four halo mass bins and three redshift snapshots. In each panel, the x-axis is the protohalo size calculated with the first centering method, and the y-axis shows those with the other three methods with vertical shifts for clarity. The dashed lines in each panel are the one-to-one reference lines. Spearman’s rank correlation coefficients for the protohalo sizes from different centering methods are presented on each panel. Here one can see that the first centering method produces the minimal protohalo size by design, as the other three methods will overestimate the sizes. Moreover, this overestimation effect has some general trends. First of all, the amplitude of the overestimation decreases with  $n$ , which is expected. Secondly, the protohalo sizes are more overestimated for larger protohalos, which can be seen from that the deviation from

the reference line is larger for larger  $x$ -values. Thirdly, such overestimation effects are larger for high- $z$  protohalos, which can be seen from the decreasing rank correlation coefficients with increasing redshift. Similarly, the overestimation effect is larger for protohalos with massive descendant halos. In summary, the overestimation effect is stronger in situations where the protohalos are less likely to be dominated by a few massive halos. Nevertheless, the rank of the protohalo size is largely preserved, since the rank correlation coefficients are  $\geq 0.85$  even when only the most massive halo is used.

## APPENDIX C: PROTOHALO SIZES USING DIFFERENT SUBHALO MEMBERSHIP DEFINITION

In the main text, we define a protohalo as the collection of progenitor halos of all subhalos in the descendant FoF halo. Alternatively, we can define a protohalo as all of the progenitor halos that will end up in descendant subhalos that are enclosed within the virial radius of the descendant halo at  $z = 0$ . Here we considered three different common halo radius defined with different density threshold values:  $R_{vir}$  defined with the threshold density in Bryan & Norman (1998),  $R_{200m}$  defined with the threshold density as  $200\Omega_m\rho_{crit}$ , and  $R_{200c}$  defined with the threshold density as  $200\rho_{crit}$ . The bottom panels of Fig. C1 show the comparison of protohalo sizes at  $z = 2$  using different definitions. Note that the dependence of protohalo size on descendant halo mass is eliminated by taking the residual with respect to the median  $\log R - \log M_0$  relation. The protohalo sizes defined with additional descendants’ halo-centric distance constraint are smaller than that defined with all descendant subhalos in the descendant FoF halo. This is expected since the progenitor halos of the subhalos on the descendant halo’s outskirts



**Figure B1.** The comparison of protohalo sizes calculated with different centers. The x-axis is the protohalo size calculated with the center of mass. The y-axis is the protohalo size calculated with the center of mass for  $n$  most massive halos in the protohalo, where  $n=1$  (blue), 2 (magenta), and 3 (red). Spearman's correlation coefficients between two protohalo sizes are shown on each panel in the corresponding color. This figure demonstrates that centering with a few most massive halos will overestimate the protohalo size, and the overestimation is larger for situations without dominating halos, such as large protohalos, high- $z$  protohalos, and protohalos with massive descendant halo mass. Nevertheless, the rank of the protohalo size is largely preserved, which is manifested by the high values of Spearman's correlation coefficients.

prefer to locate in the outer region of the protohalo, so that excluding these progenitor halos will consequently reduce the protohalo size. Nevertheless, these protohalo sizes with different definitions still strongly correlate to each other.

The top panels of Fig. C1 show the relation between the protohalo size and the central-to-total stellar mass of descendant halos with the dependence on halo mass eliminated by taking the deviation from the median value in narrow halo mass bins. Note that the calculation of  $M_{*,\text{tot}}$  only includes subhalos within the corresponding radius. After eliminating subhalos out of halo radius, the correlation coefficient between the protohalo size and the central-to-total stellar mass ratio is reduced but still as high as  $\approx 0.6$ .

#### APPENDIX D: RESULTS FOR THE ILLUSTRITNG SIMULATION

The IllustrisTNG project comprises various cosmological galaxy formation simulations with different box sizes and resolutions (Marinacci et al. 2018; Naiman et al. 2018; Nelson et al. 2018, 2019; Springel et al. 2018; Pillepich et al. 2018a,b). Here we use the one with the largest box size, which is called the TNG300 simulation, for better statistics. TNG300 simulates the formation and evolution of dark matter halos and galaxies in a box with a side length of  $205h^{-1}\text{Mpc}$ . The dark matter particle mass is about  $5.9 \times 10^7 M_\odot$ , and the mass for each gas particle is about  $1.1 \times 10^7 M_\odot$ .

Fig. D1 shows the protohalo size evolution as a function of redshift in three descendant halo mass bins. The evolution is very similar to that obtained from the ELUCID simulation (see Fig. 4). The bottom panels show the protohalos size evolution binned with the central-to-total stellar mass ratio of descendant halos,

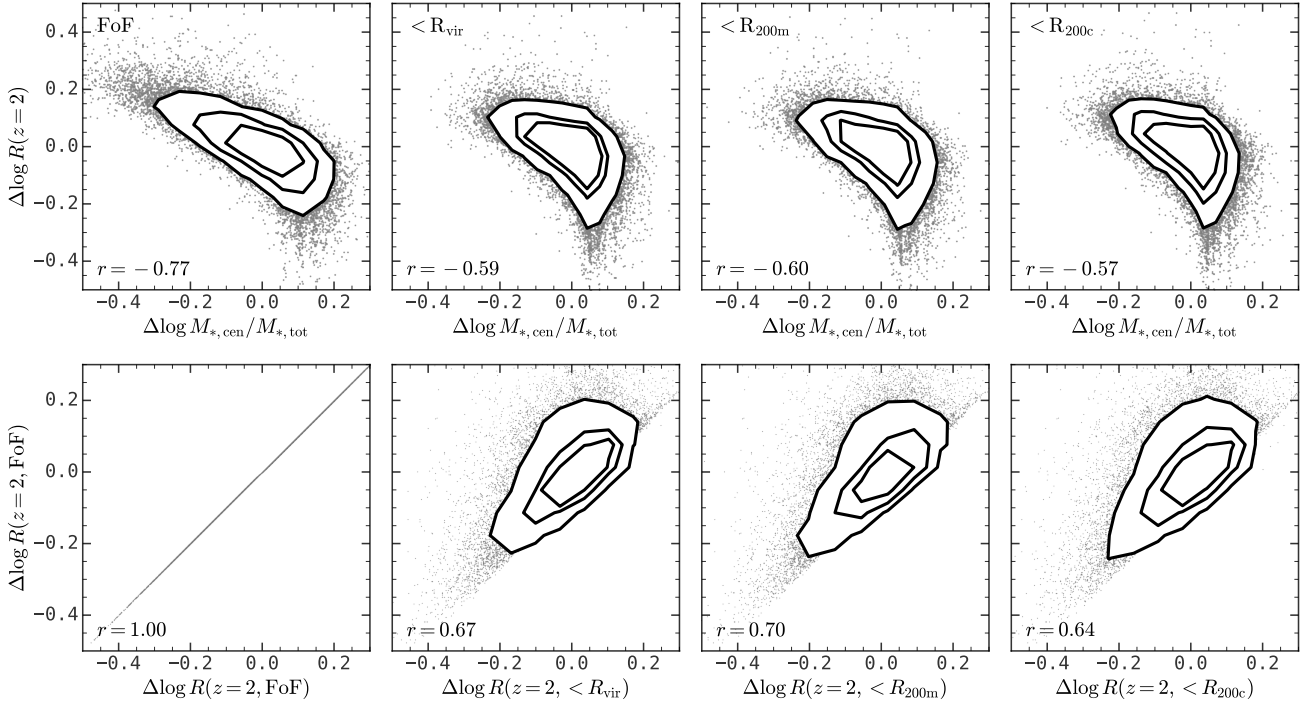


**Figure C1.** The top panels show the relation between the residual protohalo size at  $z = 2$  and the residual central-to-total stellar mass ratio at  $z = 0$  for different subhalo membership definitions for all descendant halos above  $10^{13} h^{-1} M_{\odot}$ . Similarly, the bottom panels show the comparison of the protohalo sizes at  $z = 2$ . The contour lines show encloses 50%, 70%, and 90% of all halos. The first column includes all subhalos in each FoF halo, and the second column includes only subhalos within  $R_{\text{vir}}$ . Similarly, the third and fourth columns include only subhalos within  $R_{200\text{m}}$  and  $R_{200\text{c}}$ , respectively.

$\log M_{*,\text{cen}}/M_{*,\text{tot}}$ . Here one can see that protohalos with the top-10% and bottom-10%  $M_{*,\text{cen}}/M_{*,\text{tot}}$  values differ in their size by 0.2-0.3 dex, despite the fact that the  $1 - \sigma$  range of the protohalo size is only 0.1-0.2 dex (see top panels). In addition, Fig. D2 shows the correlation between  $\log R_c$  and  $\log M_{*,\text{cen}}/M_{*,\text{tot}}$  in three halo mass bins, as well as Spearman's rank correlation coefficient, which is about 0.8. These results show that the tight correlation between the protohalo size and the central-to-total stellar mass ratio of descendant halos is also present in the IllustrisTNG simulation, where the stellar mass in each halo is obtained through hydrodynamical simulation instead of empirical modeling.

Fig. D3 shows the comparison of protohalo size calculated with equation (2) and that weighted by the stellar mass of all progenitor galaxies, which is

$$R_* = \sqrt{\frac{\sum m_{*,i} \|\mathbf{x}_{*,i} - \mathbf{x}_{\text{cen},*}\|^2}{\sum m_{*,i}}}, \quad \mathbf{x}_{\text{cen},*} \equiv \frac{\sum_i m_{*,i} \mathbf{x}_{*,i}}{\sum_i m_{*,i}} \quad (\text{D1})$$

where  $m_{*,i}$  and  $\mathbf{x}_{*,i}$  are the stellar mass and position of the  $i$ -th progenitor galaxy. Here one can see that the protohalo sizes calculated using these two different ways are highly correlated to each other, despite that the size calculated using stellar mass is systematically smaller than that of halo mass for small protohalos, which is caused by the non-constant stellar mass to halo mass ratio (Behroozi et al. 2019).

## APPENDIX E: RESULTS FOR THE MASS ACCRETION HISTORY

Here we perform similar studies on the mass accretion history as we did on the protohalo size history in § 3 and § 4.

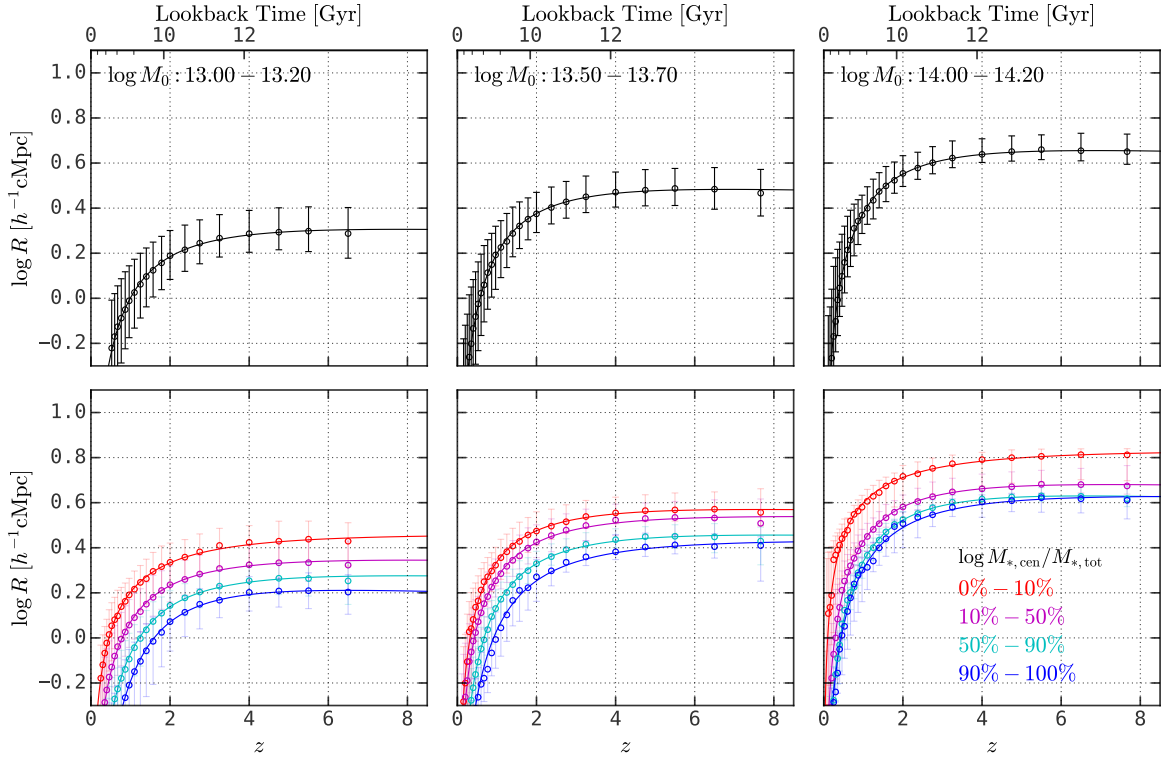
Fig. E1 shows the dependence on descendant halo mass for  $\gamma - \delta$  in equation 5 and the half-mass time  $z_{\text{half}}$ , and the relations to the central-to-total stellar mass ratio, i.e.  $\log M_{*,\text{cen}}/M_{*,\text{tot}}$ , are presented in Fig. E2. Here one can see that both  $\gamma - \delta$  and  $z_{\text{half}}$  moderately correlate with  $\log M_{*,\text{cen}}/M_{*,\text{tot}}$  for group-size halos. Halos with more dominating central galaxies tend to form earlier and have lower recent accretion rates. The correlation becomes negligible for cluster-size halos, which is consistent with the results in Wang et al. (2023). Neither of the parameters describing the mass accretion history has as a tight relation to  $\log M_{*,\text{cen}}/M_{*,\text{tot}}$  as the protohalo size history shown in Fig. 5.

Fig. E3 shows the halo assembly bias effect exhibited by the half-mass time  $z_{\text{half}}$ . The signal is rather weak, which is consistent with the results obtained in previous studies (see Gao et al. 2005; Jing et al. 2007; Mao et al. 2018).

## APPENDIX F: THE DEPENDENCE OF ASSEMBLY HISTORIES ON DESCENDANTS' NEIGHBOR COUNTS

In addition to the auto-correlation functions shown in Figs. 10 and E3, we also use the method in Mao et al. (2018) to demonstrate the difference in the halo assembly bias effect exhibited by the mass accretion history and the protohalo size history for cluster-size halos above  $10^{14} h^{-1} M_{\odot}$ . To begin with, we categorize halos into





**Figure D1.** Similar to Fig. 4, except for the TNG300 simulation.

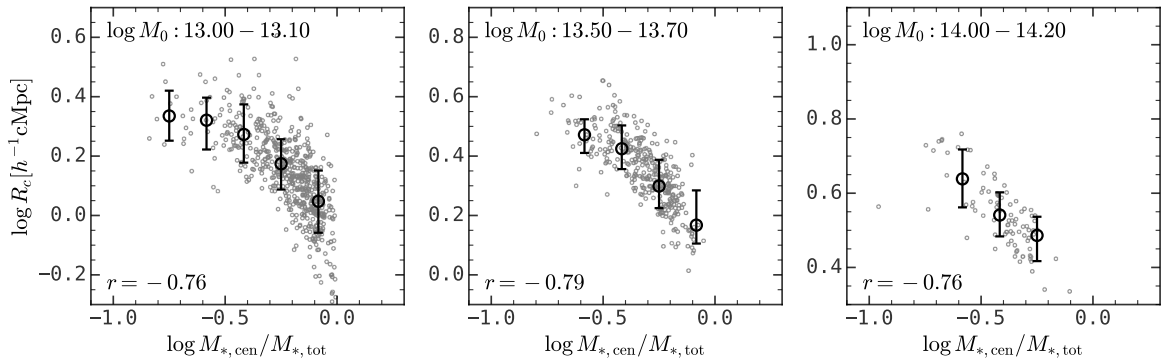


**Figure D2.** Similar to the bottom panels of Fig. 5, except for the TNG300 simulation.

different populations according to the number of another cluster-size halo within  $10h^{-1}\text{Mpc}$  of the halo in question. Specifically, halos are defined as isolated if the neighbor counts are zero. We also consider halos with  $\geq 1$  neighbors and  $\geq 2$  neighbors. We then calculate the median mass accretion history, collapsed mass history, and protohalo size history in each category, as presented in Fig. F1. Here the collapsed mass history is defined as the total progenitor halo mass above  $fM_0$  with  $f = 0.02$  as a function of redshift (e.g. Neto et al. 2007; Li et al. 2008; Gao et al. 2008; Ludlow et al. 2016). The fractional deviation relative to the results obtained for the parent halo sample is presented on the bottom panels. Note that the collapsed mass history drops below  $0.02M_0$  above  $z \approx 3$ . This figure demonstrates that isolated halos exhibit nearly identical mass

accretion history and collapsed mass history to the paired halos with more than one and two neighbors (Li et al. 2008). In contrast, paired halos exhibit larger protohalo sizes than isolated halos, and the fractional difference is about 5% for halos with  $\geq 1$  neighbors, and 10% for halos with  $\geq 2$  neighbors.

Fig. F1 contain different information about the halo assembly bias from Figs. 10 and E3. The auto-correlation function characterizes the halo assembly bias on different scales, but it requires a further compression from a linear structure of history to a scalar, which are  $z_{\text{half}}$  and  $\log R_c$  in this case. In contrast, Fig. F1 compares the whole mass accretion history and protohalo size history for paired and unpaired halos, but this comparison is made on the chosen scale, which is  $10h^{-1}\text{Mpc}$  in our case. Therefore, Fig. F1

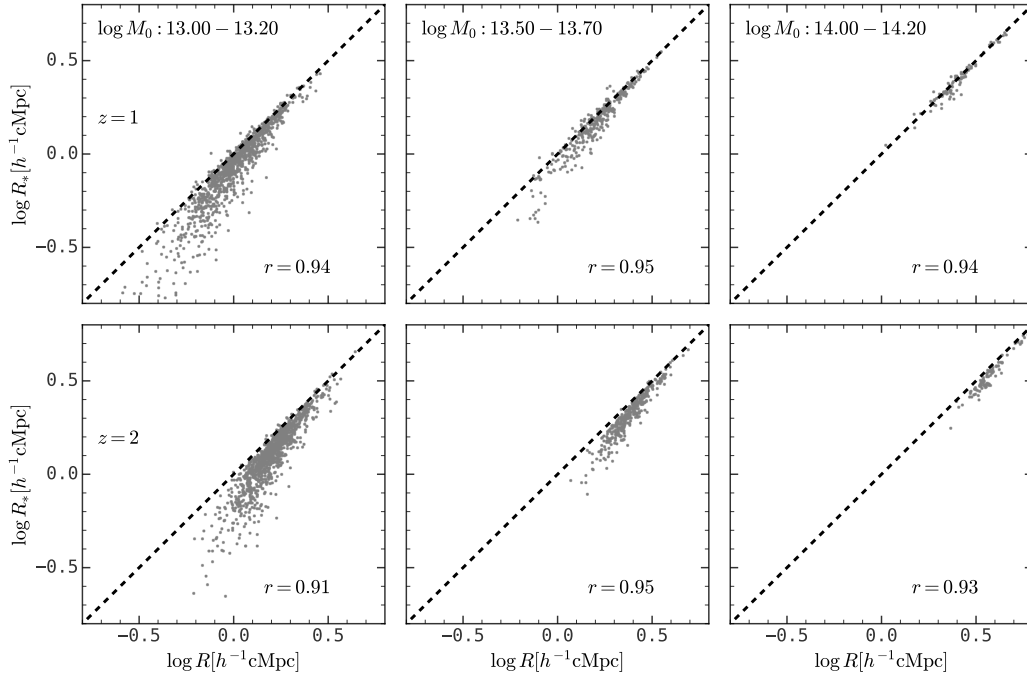


**Figure D3.** The comparison of protohalo size calculated with halo mass ( $x$ -axis) and stellar mass ( $y$ -axis) in TNG300 at  $z = 1$  and  $z = 2$ . Spearman's rank correlation coefficients are labelled at the lower right corner of each panel. This figure demonstrates that the protohalo sizes calculated using halo mass and stellar mass are highly correlated to each other, despite that the size calculated using stellar mass is systematically smaller than that of halo mass for small protohalos.

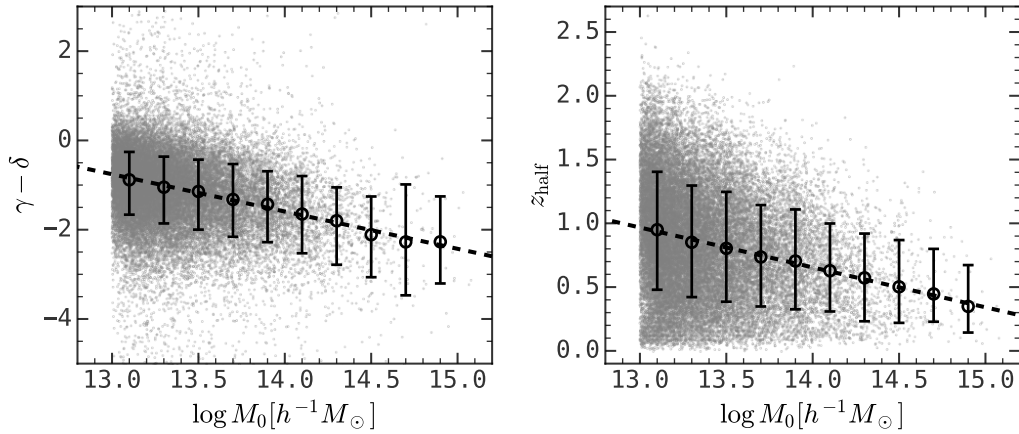


**Figure E1.** Similar to Fig. 3, except for  $\gamma - \delta$  and  $z_{\text{half}}$ .

shows that not only  $z_{\text{half}}$ , but also the whole mass accretion history contains no information about the halo assembly bias.

This paper has been typeset from a  $\text{\TeX}/\text{\LaTeX}$  file prepared by the author.

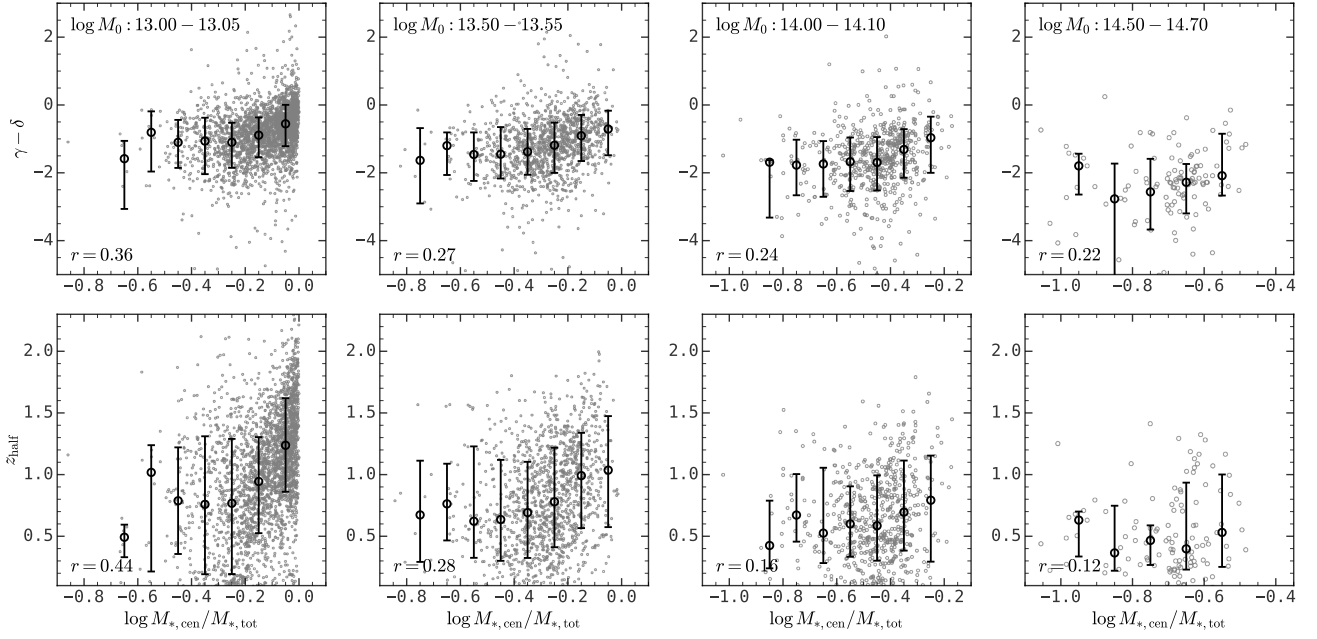


**Figure E2.** Similar to Fig. 5, except for  $\gamma - \delta$  and  $z_{\text{half}}$ .

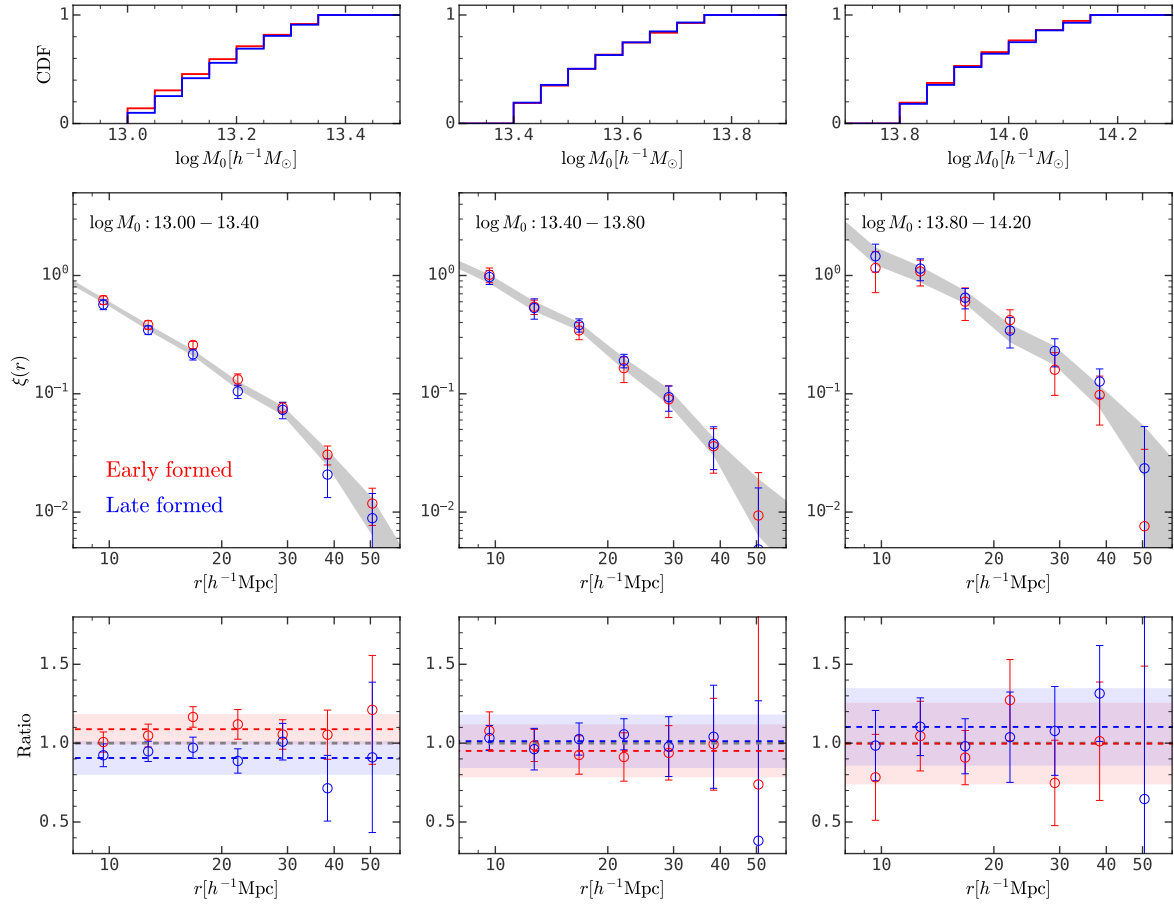


**Figure E3.** Similar to Fig. 10, except that subsamples here are divided according to their  $z_{\text{half}}$ . This figure shows that the halo assembly bias from the halo formation time is negligible for massive halos.

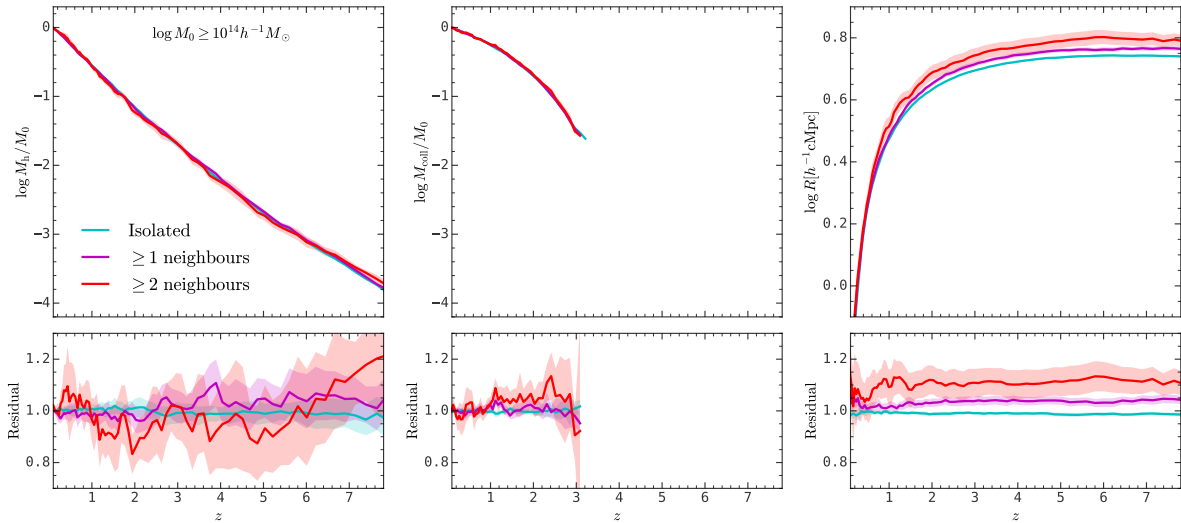


**Figure F1.** The top panels show the median mass accretion histories, collapsed mass history, and protogalaxy size histories for halos above  $10^{14} h^{-1} M_{\odot}$  and different numbers of neighbours within  $10 h^{-1} \text{Mpc}$ . The bottom panels show the fractional difference between three subsamples with different neighbor counts and the parent sample. The shaded regions show the standard deviation estimated from the bootstrap samples. This figure shows that the protogalaxy size history has a significant dependence on the surrounding environment of halos, but such dependence for the mass accretion history and the collapsed mass history is negligible.